



Applied Mechanics Research Group

Department of civil engineering

MSc Thesis:

# Geometric Analysis of Trapezoidal Hills Subject to Vertically Incident $SH$ waves

A Thesis submitted by Susana Velez Zuluaga for the degree of Master in Science in Universidad Eafit

---

Supervised by:  
Juan David Gomez

# Geometric Analysis of Trapezoidal Hills Subject to Vertically Incident $SH$ waves

Susana Vélez Zuluaga

November 28, 2014

## Abstract

Topographic effects have been shown to play a significant role on the local ground response during earthquakes. However, due to the large number of involved parameters the problem is rarely considered in seismic design regulations. Recently, there has been a tremendous development by the engineering community, regarding methods and computational infrastructure to address the problem via numerical simulations. Although numerically based models may give accurate results when fed with appropriate field data, the obtained solutions are still very limited and strongly dependent on unknown factors like the input excitation. Therefore, there is a clear need to develop strong conceptual understanding allowing practising engineers to arrive at first order approximations, useful to validate complex numerical solutions. In this work we explore the use of purely geometrical methods in the determination of the dynamic response of trapezoidal geometries to vertically incident horizontally polarized shear waves. The geometries may be considered representative of hills or earth embankments, depending on its characteristic dimensions. The hill response is first found with a frequency domain based boundary element code and the results are later analysed using a geometric approach, where the solution is partitioned into incident and reflected rays, forming the incoming or optical field, and the diffraction contribution. This last term is obtained with a technique available from the literature. The analysis corresponding to the optical field, reveals that there are only 5 possible scenarios or different solutions and that any given hill can be classified into one of these five possible cases. Depending upon the dimensionless frequency of the problem (relating incident wavelength to the hill characteristic dimension), the solution is found to be governed by the optical solution or by the contribution from the diffraction terms. The results are first presented in terms of frequency amplitude functions since that description facilitates the analysis by geometric methods, however for completeness, the resulting transfer functions are later used to obtain results in the time domain representative of typical numerical solutions as the ones derived with commercial computational software.

**Keywords:** Topographic effects, Site effects, Wave propagation, Superposition based diffraction.

## 1 Introduction

Recorded seismic events have shown that the amplitude and frequency content of earthquake induced ground motions can be significantly modified by topography. Well known examples are identified in the 1971-San Fernando, California earthquake; the 1994-Northridge, California earthquake (Sepúlveda et al., 2005); the 1995-Kobe, Japan earthquake (Kawase, 1996; Pitarka et al., 1998); the 1999-Eje-cafetero Colombia earthquake, (Restrepo & Cowan, 2000); the 1999-Athens Greece earthquake (Tselentis & Zahradnik, 2000); and the 2011-Christchurch New Zealand earthquake (Kaiser et al., 2012). Several theoretical studies have been conducted over the past decades trying to understand, reproduce

and predict site responses considering topographic effects. Although these studies have been successful at qualitatively predicting zones of higher amplification, there are still important quantitative differences when the results are compared to actual field data. For instance [Furumura & Koketsu \(1998\)](#) with regards to the 1995-Kobe earthquake pointed out *"The result simulates the shape of the damage belt fairly well, though the peak ground velocities are only half of those observed"*.

The access to high performance computers and advances in computational mechanics techniques have given scientists the opportunity to construct models with increased levels of complexity such as dynamic rupture mechanisms, propagation through layered media, non-linear soil response and three-dimensional realistic topographies ([Furumura & Koketsu, 1998](#); [Ma et al., 2007](#); [Lee et al., 2009](#); [Restrepo et al., 2012](#); [Nakamura et al., 2012](#); [Furumura & Koketsu, 1998](#); [Restrepo, 2013](#)). Despite these complexities, numerical results and predicted intensity levels are still far from understood in a way that they can be thoroughly considered in seismic design regulations. Although the use of robust numerical based models is becoming a promising technique, there is still an important gap in understanding fundamental aspects of the problem. In this work we study the problem of topographic site effects from a rather simplistic perspective. We focus on the analysis of trapezoidal hills, submitted to vertically incident horizontally polarized shear waves, studied from a geometric point of view and with analysis methods operating in the frequency domain which allows us to approach the problem using methods based on the optical theory of rays.

Previous works involving simple topographies in two dimensions (2D) describe geometries resembling the shape of valleys, canyons, hills, mountains and other configurations of significance in engineering, such as slopes, dams and embankments. Particular geometries that have been commonly studied are semi-cylindrical canyons and valleys ([Trifunac, 1972, 1971](#)); trapezoidal canyons and valleys ([Moczo et al., 1997](#); [Gelagoti et al., 2012](#)); V-shaped canyons [Takemiya & Fujiwara \(1994\)](#) and slopes [Nguyen & Gatmiri \(2007\)](#); circular hills [Kawase & Aki \(1990\)](#); and trapezoidal hills [Kamalian et al. \(2008\)](#), among others. Moreover general rule-of-thumb guidelines to consider topographic effects have emerged from analysis conducted over these simple geometries. For instance [Assimaki et al. \(2005\)](#) concluded that amplifications are observed near the crest and de-amplifications appear near the toe while other complex amplification patterns appear on hill slopes. [Bard \(1997\)](#), connected these results to three physical phenomena, namely; (i) the influence of the incidence angle (ii) focusing and defocusing of incident and reflected waves and (iii) surface and diffracted waves propagating through the topography.

A slope is a simple fundamental geometry that has been widely used for investigating topographic effects since its shape is found in different engineering configurations (e.g., hills, canyons, basins, etc). A trapezoidal hill can be understood as the intersection of two finite sized slopes. Models with different combinations of the geometric features of the slope have been used in parametric studies describing the effect of these geometries in the total response. For instance, [Ashford et al. \(1997\)](#) propagated harmonic  $SH$  and  $SV$  waves for frequencies between  $0.5 - 10Hz$  over slopes with steeped layers of soil resting over a visco-elastic half-space where the slope angle varied from  $30^\circ$  to  $90^\circ$  using the finite element method (FEM). Results were shown in terms of the dimensionless frequency  $h/\lambda$ , where  $h$  is a characteristic slope dimension and  $\lambda$  is the dominant wavelength of the input excitation. These authors concluded that the topographic effect is stronger for slopes steeper than  $60^\circ$  and tends to decrease with slope angle. Similar works using FEMs are due to [Assimaki et al. \(2005\)](#) who evaluated the effects of local soil conditions on the diffraction mechanism near the vertex of cliff type topographies during the 1999-Athens earthquake. In that work vertically incident  $SV$  waves in the form of a Ricker pulse were propagated in order to describe the ground motions in a single and two-layered cliff resting over a half-space. These authors pointed out that *"the effects of local soil conditions have been shown to affect the spatial distribution, aggravation level, and frequency content of the surface response next to the crest"*. Similar studies for trapezoidal hills were developed

by (Moczo et al., 1997; Razmkhah et al., 2007; Kamalian et al., 2008; Amelsakhi et al., 2014), in which modifications to the response caused by the presence of the hill were identified. In similar studies found in the literature, for both slopes and trapezoidal hills, it has been recognized that geometric parameters like the slope height, inclination angle and dimensionless frequency control the total ground response.

In this work and motivated by previous results based on simplified topographies, we approach the problem from a geometric point of view in an effort to connect the general observations reported in these studies with physical aspects of the response that can be applied in more general scenarios. The study is conducted in the frequency domain and over a family of trapezoidal hills subjected to vertically incident  $SH$  waves. For that purpose we use as analysis technique a superposition based diffraction (SBD) method where the total solution is split into a contribution from waves generated by diffraction sources existing in the hill geometry, and from the optical field, described by incident and reflected rays. The geometric analysis is expected to shed light into the connection between the total response and the geometric parameters of the hill, namely its width  $a$ , slope angle  $\beta$  and height  $h$ . In order to use the SBD technique as analysis method, we first obtain the total solution by a numerical boundary element method (BEM). In a subsequent analysis we proceed to separate the optical ray theory solution from the total response (computed numerically) and compute in this way the contribution from the diffraction field. This last term is then conceptually analysed with the aid of the diffraction technique. From the geometric analysis conducted mainly on the basis of the optical field it is found that there are only five parametric configurations encompassing all the possible propagation scenarios. We classify these five scenarios according to the complexity involved in the level of interaction between the incoming motion and the geometry of the hill. Depending on the dimensionless frequency of the problem, it is also found that the solution may be approximated by the optical or the diffracted field alone. This result is relevant in the derivation of first order approximations for the consideration of site effects at the engineering level.

The report is organized as follows. In the first part, following this introduction, we describe the analysis technique based on the superposition of diffracted and incoming rays. The presentation of the analysis method closely follows the one used by Gomez et al. (2013) while the superposition technique has been proposed by Jaramillo et al. (2012). In particular, we describe how to apply the method in the solution of the trapezoidal hill. In the second section we describe briefly the used boundary element method formulation used to compute the total solution in the frequency domain. Results describing the analysed geometry and showing general observations from the frequency and time domain analysis are presented next. The report finishes with a section resuming the main conclusions from the study.

## 2 Methods

### 2.1 The Superposition Based Diffraction Technique

This section describes the basis of the superposition based diffraction (SBD) approach. The basis of the analysis technique, originally developed in Jaramillo et al. (2012), is the linear character of the scattering problem which allows the total solution to be written in terms of the addition of different and arbitrary superpositions. One such partition is based upon the usual earthquake engineering definition of free-field motion, where the total response is constructed by the addition of an incident field  $u^{IN}$ ; its reflections in a half-space with the scatterer being removed  $u_A^R$ ; and a scattered field  $u_A^S$ . Considering the common earthquake engineering definition of free field motion given by  $u_A^0 \equiv u^{IN} + u_A^R$  allows us to write this total field like;

$$u^T = u_A^0 + u_A^S \quad (1)$$

where  $u^T$  corresponds to the total response and by reasons that will become apparent later, we refer to the free-field term  $u_A^0$  like the artificial incoming motion.

An alternative partition of the field, introduced in [Gomez et al. \(2013\)](#), and constituting the basis of the method is now explained with reference to fig. 1 which schematically describes a scatterer problem where the domain has been partitioned into the supporting half-space  $\Omega^+$  (top-right) and the scatterer  $\Omega$  (bottom-right) respectively.

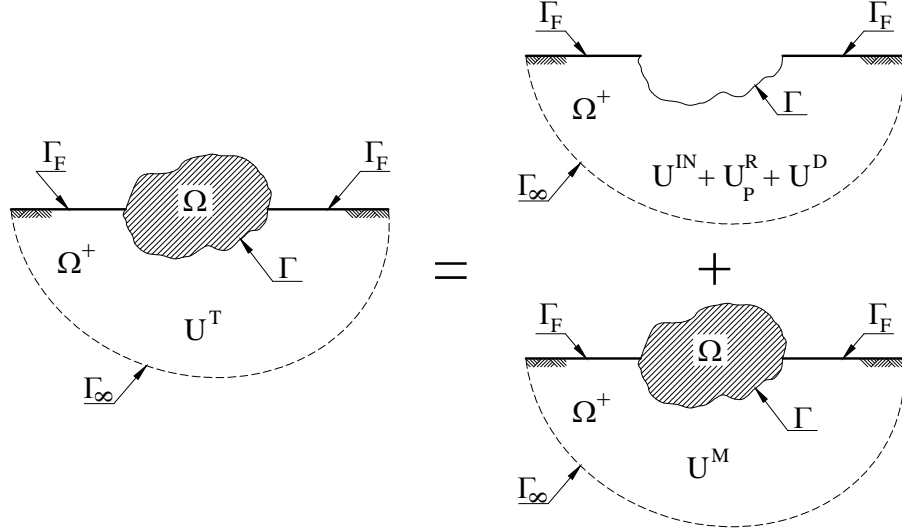


Figure 1: Partition of the domain.

Based on the above sub-domain partition we can subsequently write for the total field;

$$u^T = u^{IN} + u_P^R + u^D + u^M \quad (2)$$

where the first three terms correspond respectively to the incident field, its reflections over the free-surface  $\Gamma$  which is exposed after removing the scatterer from the half-space and the diffracted field required to restore continuity on the component  $u^{IN} + u_P^R$ . If we identify this last part of the solution like the optical field  $u_P^0$  or physically based incoming motion we can re-write the total solution like;

$$u^T = u_P^0 + u^D + u^M. \quad (3)$$

In eq. (3)  $u^M$  is an additional field introduced by the scatterer  $\Omega$ . The name artificial incoming motion, coined to the engineering free-field definition  $u_A^0$  is now evident since such definition, according to eq. (1), leads to the concept of the scattered field which has mainly a mathematical meaning. If we now consider the term  $u^D + u^M$  like an alternative scattered motion or relative displacement  $u_P^S$  between the total solution and the optical field, then eq. (3) can be written like;

$$u^T = u_P^0 + u_P^S \quad (4)$$

which is analogous to the classical partition given by eq. (1) in terms of the free-field and the mathematical scattered motion. The alternative and classical scattered fields are easily shown to be connected like;

$$u^S = u_P^R - u_A^R + u_P^S. \quad (5)$$

In problems involving only a topographic irregularity where  $u^M = 0$  and  $u_P^S = u^D$  the total field can be written like;

$$u^T = u_P^0 + u^D. \quad (6)$$

Since the optical field (OF) or physically based incoming motion  $u_P^0$ , can be obtained analytically, the construction of the total solution becomes feasible as long as we find a way to compute the contribution from the diffracted field. This term can be obtained following the work from [Jaramillo et al. \(2012\)](#) in terms of the diffracted field for a generalized infinite wedge, and after representing the topographic irregularity as a superposition of wedges of different inclinations and perceiving the incident wave at different angles. Although the formulation of the problem in the standard form of eq. (1) is more suitable for numerical treatments of the problem, the superposition given by eq. (6) has a stronger physical basis and turns out to be highly convenient for an analytical approach.

## Fundamental solution

The fundamental wedge and the corresponding diffraction field generating the terms  $u^D$  in eq. (6) and constituting the basis of the SBD technique developed by [Jaramillo et al. \(2012\)](#) are given in fig. 2 and eq. (7) respectively. The diffraction contribution is considered using the well established geometrical theory of diffraction (GTD), originally proposed by [Keller \(1956\)](#) who found the diffraction associated to a generalized infinite wedge under a plane or cylindrical  $SH$  wave.

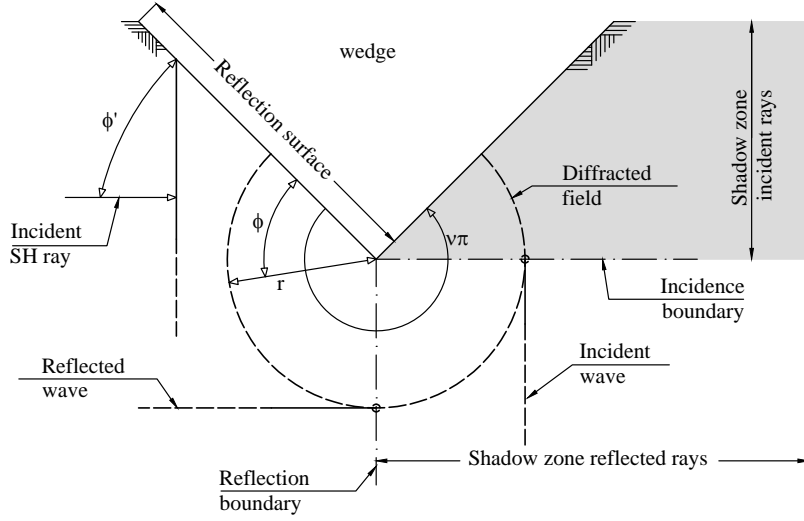


Figure 2: Plane  $SH$  wave incident against an infinite wedge. The region of existence of the incident rays corresponds to the illuminated zone. As the incident front is reflected by the free surface a zone illuminated by the reflected rays develops. The superposition of these two fields is discontinuous, however continuity is restored by the cylindrical diffracted field that penetrates into the shadow zone.

$$\begin{aligned}
u^D(\phi, r) = A \frac{-e^{(-i(kr+\pi/4))}}{2\nu\sqrt{2\pi}\sqrt{kr}} & \left[ \cot\left(\frac{\pi+(\phi-\phi')}{2\nu}\right) F(kLa^+(\phi-\phi')) \right. \\
& + \cot\left(\frac{\pi-(\phi-\phi')}{2\nu}\right) F(kLa^-(\phi-\phi')) \\
& + \cot\left(\frac{\pi+(\phi+\phi')}{2\nu}\right) F(kLa^+(\phi+\phi')) \\
& \left. + \cot\left(\frac{\pi-(\phi+\phi')}{2\nu}\right) F(kLa^-(\phi+\phi')) \right] \quad (7)
\end{aligned}$$

where  $r$  =radial coordinate to the field point measured from the vertex of the wedge,  $\phi$  = angular coordinate measured with respect to the reflection surface,  $\phi'$  =incidence angle measured with respect to the reflection boundary,  $\nu\pi$  =wedge angle,  $r'$  =radius of the incident cylindrical wave (for the diffraction of a cylindrical front),  $k$  =wave number and  $\beta$  =velocity of wave propagation. For a complete discussion of the remaining terms appearing in eq. (7) the reader is referred to [Jaramillo et al. \(2012\)](#). These terms correspond to:

$$\begin{aligned}
F(X) &= 2i\sqrt{X}e^{\hat{i}X} \int_{\sqrt{X}}^{\infty} e^{-i\tau^2} d\tau \\
L &= r \quad \text{for incident plane waves} \\
L &= \frac{rr'}{r+r'} \quad \text{for incident cylindrical waves} \\
a^{\pm}(\theta) &= 2 \cos^2\left(\frac{2\nu\pi N^{\pm} - \theta}{2}\right) \\
N^+ &= \begin{cases} 0 & \text{if } \theta \leq \nu\pi - \pi \\ 1 & \text{if } \theta > \nu\pi - \pi \end{cases}, \quad N^- = \begin{cases} -1 & \text{if } \theta < \pi - \nu\pi \\ 0 & \text{if } \pi - \nu\pi \leq \theta \leq \pi + \nu\pi \\ 1 & \text{if } \theta > \pi + \nu\pi \end{cases}
\end{aligned}$$

### Application of the SBD method to a trapezoidal hill

The fundamental solution described in the previous section, facilitates the computation of the total displacement for any geometry that can be decomposed into multiple wedges. This is accomplished by adding the diffracted field  $u^D$  (see eq. (7)), to the optical or ray theory solution  $u^0$ .

In fig. 3 a trapezoidal hill is decomposed into the four infinite wedges labelled (A),(B),(C) and (D). Each one of these wedges becomes a source of diffracted waves. Thus as an incident wave front interacts with the wedge the source contributes with terms of the type  $u^D$  computed according to eq. (7). If the interacting wave belongs to the optical field the  $u^D$  term is a primary diffracted wave. On the other hand if the interacting wave corresponds to a previously generated diffracted wave the  $u^D$  term is a higher order diffracted wave. These first and higher order diffracted waves together with its corresponding reflections at free surfaces are illustrated in fig. 4 and fig. 5.

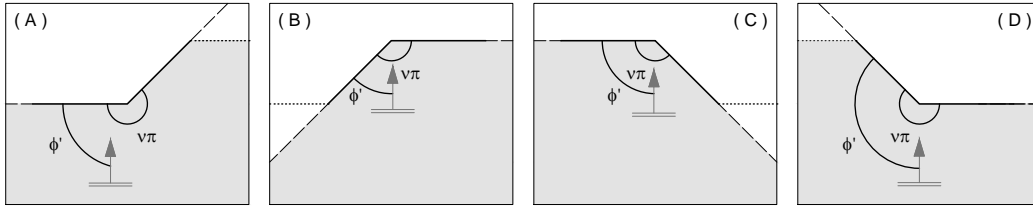


Figure 3: Diffraction sources for an embankment shaped geometry.

First order diffraction is generated when any component of the optical field reaches a diffraction source, filling the discontinuities of the optical field. In particular fig. 4 illustrates how the incident and reflected fields are completed by first order diffraction. It should be noticed that there is a discontinuity along the extension of the slopes, where the limits of the infinite wedges (B) and (C) are defined. Beyond these limits any diffraction front generated at (B) and (C) is nonexistent.

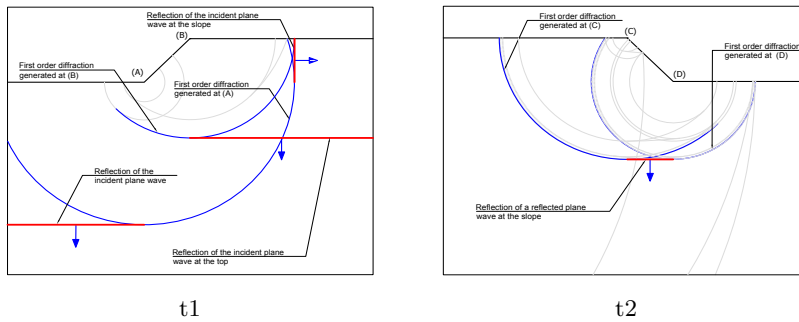
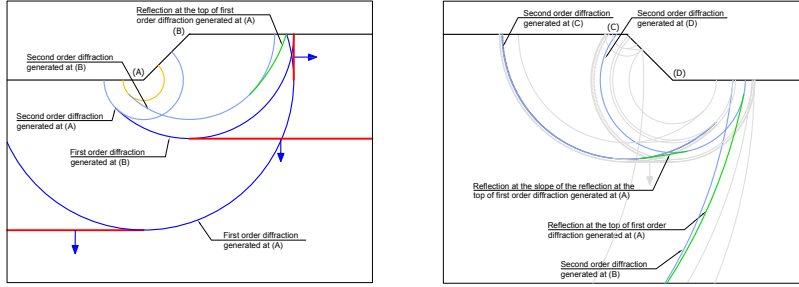


Figure 4: Incident and reflected field discontinuities filled by first order diffraction

Similarly, higher order diffraction terms are generated when any diffraction waves reaches a wedge. These terms complete the discontinuities of other parts of the diffracted field, such as the discontinuity along the extension of the slope mentioned above. Figure 5 schematically shows how second order diffraction completes the discontinuities corresponding to:

- The first order diffraction generated at source (B) due to the infinite wedge limit.
- The reflection at the top of the hill of the first order diffraction generated at source (A) .
- The reflection at one of the slopes of the reflection of the first order diffraction generated at (A), at the top of the hill.



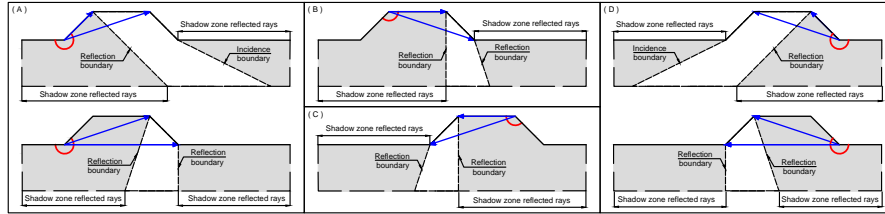


Second order diffraction completes the discontinuities of the first order diffraction generated at source (B) and the reflection at the top of the first order diffraction generated at source (A).

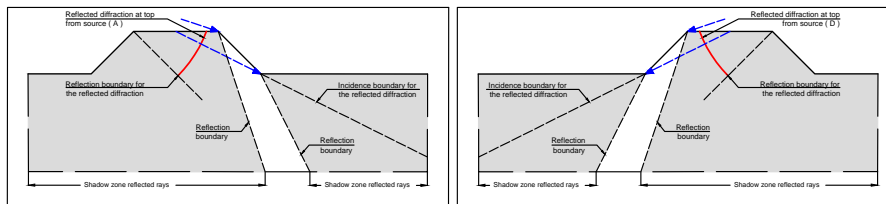
Second order diffraction completes the discontinuities of the reflection at the top of the first order diffraction generated at source (A) and its reflection at the slope.

Figure 5: Diffracted field discontinuities filled by higher order diffraction

The last type of diffraction is related with the interactions (i.e., reflections) of the diffracted field with the different free surfaces forming the topographic irregularity. These reflected fronts are discontinuous at reflection boundaries where continuity is restored by the higher order diffraction terms. Figure 6 displays the reflection boundaries of the reflected diffractions for a hill with  $\beta = 45^\circ$ .



Reflection boundaries of a diffraction terms first reflection at the slopes and top of the hill



Reflection boundaries of a diffraction terms second reflection at the slopes of the hill

Figure 6: Diffraction terms related with the interaction of other diffraction terms with the surface

Except for the first order diffraction, each type of diffraction is repeated infinitely as long as the diffractions interact with the geometry.

## 2.2 Boundary Elements Method

The response of the trapezoidal hill was found using the representation theorem described by [Banerjee & Butterfield \(1981\)](#), following the procedure developed by [Pao & Varatharajulu \(1976\)](#) to find the scattering field by a surface of discontinuity caused by an obstacle of volume  $V_1$  enclosed by surface  $S$  as shown in fig. 7. The media outside the obstacle or scatterer is an homogeneous isotropic half-space with a traction free surface. In the particular problem at hand the scattering of the incident waves is produced by the presence of the trapezoidal hill.

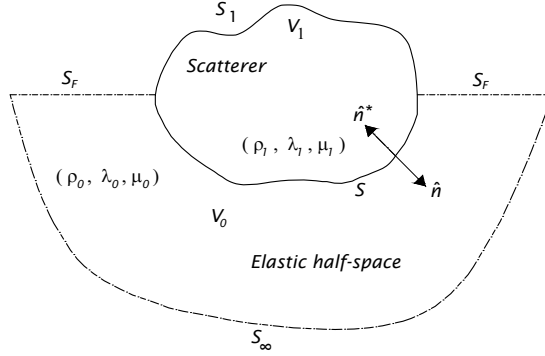


Figure 7: Definition of the boundary problem domain

The total response is the superposition of incoming and scattered waves as expressed in eq. (8).

$$u = u^0 + u^S \quad (8)$$

The Boundary Value Problem (with a time dependence term  $e^{i\omega t}$ , implicit in all the expressions from now on), governing the total response inside the half-space ( $V_0$ ) and the topographic irregularity ( $V_1$ ) can be formulated via an integral representation theorem as follows:

$$\int_S G_{ij}^{HS}(\vec{x}, \hat{i}\omega; \vec{\xi}) t_j(\vec{x}, \hat{i}\omega; \hat{n}^*) dS(\vec{x}) - \int_S H_{ij}^{HS}(\vec{x}, \hat{i}\omega, \hat{n}^*; \vec{\xi}) u_j(\vec{x}, \hat{i}\omega) dS(\vec{x}) + u_i^0(\vec{\xi}, \hat{i}\omega) = u_i(\vec{\xi}, \hat{i}\omega) \quad , \quad \vec{\xi} \in V_0 \quad (9)$$

$$\int_{S_1} G_{ij}^{FS}(\vec{x}, \hat{i}\omega; \vec{\xi}) t_j(\vec{x}, \hat{i}\omega; \hat{n}) dS_1(\vec{x}) - \int_{S_1} H_{ij}^{FS}(\vec{x}, \hat{i}\omega, \hat{n}; \vec{\xi}) u_j(\vec{x}, \hat{i}\omega) dS_1(\vec{x}) = u_i(\vec{\xi}, \hat{i}\omega) \quad , \quad \vec{\xi} \in V_1 \quad (10)$$

Where  $G_{ij}^{HS}(\vec{x}, \hat{i}\omega; \vec{\xi})$  and  $H_{ij}^{HS}(\vec{x}, \hat{i}\omega, \hat{n}^*; \vec{\xi})$  are the displacement and traction Green's tensors for a half-space, and  $G_{ij}^{FS}(\vec{x}, \hat{i}\omega; \vec{\xi})$  and  $H_{ij}^{FS}(\vec{x}, \hat{i}\omega, \hat{n}; \vec{\xi})$  are the displacement and traction Green's tensors for a full-space.

In order to find the total displacement  $u_i(\vec{\xi}, \hat{i}\omega)$  along the surface, eq. (10) and eq. (9) are solved numerically using the BEM algorithm *Damian* developed by [Jaramillo \(2014\)](#)

and where the boundaries  $S_1$  and  $S$  are discretized into  $K_1$  and  $K$  segments, respectively and traction and displacements are assumed to be constant along each segment. The discrete form of eq. (10) and eq. (9) are:

$$u_i(\vec{\xi}, \hat{i}\omega) + \sum_{k=1}^K \left[ u_j(k, \hat{i}\omega) \int_{S_k} H_{ij}^{HS}(\vec{x}, \hat{i}\omega, \hat{n}^*; \vec{\xi}) dS_k \right] - \sum_{k=1}^K \left[ t_j(k, \hat{i}\omega; \hat{n}^*) \int_{S_k} G_{ij}^{HS}(\vec{x}, \hat{i}\omega; \vec{\xi}) dS_k \right] = u_i^0(\vec{\xi}, \hat{i}\omega) \text{ for } \vec{\xi} \in V_0 \quad (11)$$

$$u_i(\vec{\xi}, \hat{i}\omega) + \sum_{k=1}^{K_1} \left[ u_j(k, \hat{i}\omega) \int_{S_k} H_{ij}^{FS}(\vec{x}, \hat{i}\omega, \hat{n}; \vec{\xi}) dS_k \right] - \sum_{k=1}^{K_1} \left[ t_j(k, \hat{i}\omega; \hat{n}) \int_{S_k} G_{ij}^{FS}(\vec{x}, \hat{i}\omega; \vec{\xi}) dS_k \right] = 0 \text{ for } \vec{\xi} \in V_1 \quad (12)$$

After solving eq. (11) and eq. (12) for the total response along the surface, the response at any point inside the boundary may be found using the same equations.

### 3 Results

We obtained the response of a family of trapezoidal hills subjected to vertically incident *SH* waves. The total field was initially computed using the frequency domain boundary-element-method-based algorithm described previously. The response in each topographic irregularity was then analyzed using the superposition based diffraction technique, where the field is separated into incident and reflected frequency independent rays and the frequency dependent diffracted field. From the propagation patterns generated by the optical field, we were able to identify 5 combinations of geometrical parameters comprising all possible scenarios. In order to qualify each scenario, we introduced the idea of level of complexity in the propagation pattern, where a low level of complexity means a low degree of interaction between the hill and the optical field. Each identified level of complexity was characterized by a set of segments and points over the free surface where focusing of rays occurs and over which bounding values in the amplitude function can be anticipated. We also found simple expressions to fully locate the different segments and to study its variation with the slope angle for hills of different aspect ratio. These parametric analysis were described graphically with the idea of producing an engineering tool to conduct first order calculations based solely on the optical field.

#### 3.1 Problem description

A typical hill, fully characterized by the crest width  $a$ , height  $h$  and slope angle  $\beta$  is shown in fig. 8. The material is described by the shear wave propagation velocity  $c_t = 1.0km/s$  and mass density  $\rho = 1000kg/m^3$ . On the other hand, anticipating our needs for the response analysis to be conducted with the aid of the superposition based diffraction technique, it is convenient to introduce as an additional parameter the internal angle  $\alpha$  given by;

$$S_\alpha = \frac{a/2 + b}{\sqrt{h^2 + (a/2 + b)^2}}. \quad (13)$$

This angle, which is a function of  $a$ ,  $h$  and  $\beta$ , actually controls the location of the reflection and incidence boundaries where the discontinuous optical and diffracted field are coupled to restore a total continuous solution.

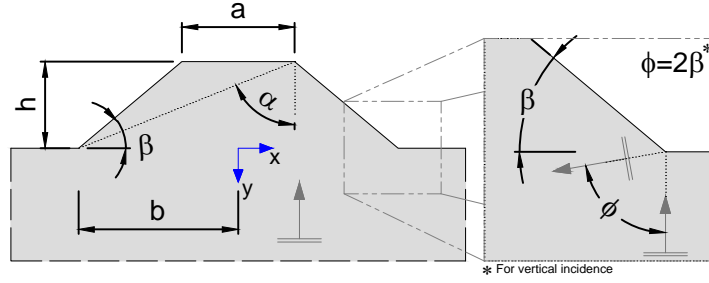


Figure 8: A typical hill used in this study. The internal angle  $\alpha$  controls the incidence and reflection boundaries of the optical field

The frequency domain response for each hill was described in terms of the displacement amplitude  $\| U(i\omega) \|$  after assuming monochromatic plane incident waves of unit amplitude. The results are given in terms of normalized frequency  $\eta = f_i * h / c_t = h / \lambda_i$  where  $f_i$  is frequency for the  $i$ -th wave and  $\lambda_i$  its corresponding wavelength. In order to study the different propagation patterns we also computed time domain results after inverse Fourier transforming the product of frequency domain transfer function with an input Fourier spectra for a Ricker pulse of central frequency  $f_c$  and time domain description given by;

$$R(t) = (2 * (\pi * (t - t_o) * f_c) - 1) e^{-(\pi * (t - t_o) * f_c)^2} \quad (14)$$

where  $t_o$  is a time parameter related to the peak in the pulse amplitude.

The frequency domain response for all the hills considered in this study was determined using the boundary element method based algorithm previously described. A typical mesh is shown in fig. 9. The specific algorithm uses a half-space Green's function in order to represent the radiation boundary condition and a full-space Green's function to describe the scatterer which in this case corresponds to the hill. The mesh shown in the figure also includes observation points along the free surface of the half-space in order to obtain the final response once the unknown displacements have been predicted. In the used algorithm we used constant elements with characteristic size corresponding to  $\lambda_{min}/10$ .

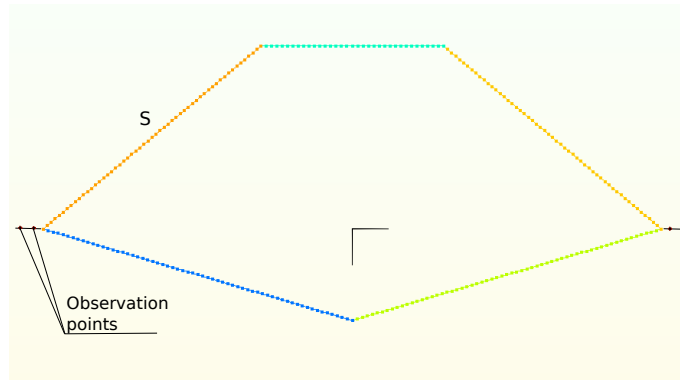


Figure 9: Mesh along the surface  $S$ , surrounding the topographic irregularity of trapezoidal shape

### 3.2 Propagation pattern associated to the optical field

Figure 10 shows the ray diagram associated to the optical field  $u^0$  resulting from the superposition of the vertically incident  $SH$  wave and its multiple reflections  $u^R$  over the free surface of the hill. This particular case corresponds to a hill with an aspect ratio  $a/h = 1.67$  and slope angle  $\beta = 50^\circ$ . The set of parallel lines extending throughout the domain correspond to incident and reflection boundaries where the optical field exhibits discontinuities that must be smoothed out by the diffraction contribution. The different points and its associated rays are used to illustrate the propagation patterns in the different regions. Accordingly, the shown rays correspond to finite fronts travelling in different directions. Over the free surface we have also marked segments describing zones illuminated by more than two rays and where the amplitude function is expected to attain values larger than those in the free-field. In what follows we refer to these segments as concentration segments where the labels  $L_{S_i}$  and  $L_{T_i}$  indicate whether the segment is located over the sloped or over the top part of the hill. For instance concentration segment  $L_{T3}$ , fully covering the crest, is illuminated by the main incident front and by the rays reflected by each one of the slopes thus conforming a six-rays-system over the free surface. The particular character of the interference among these 6 rays dictates bounding values of 6.0 and 4.0 for the amplitude function over this region.

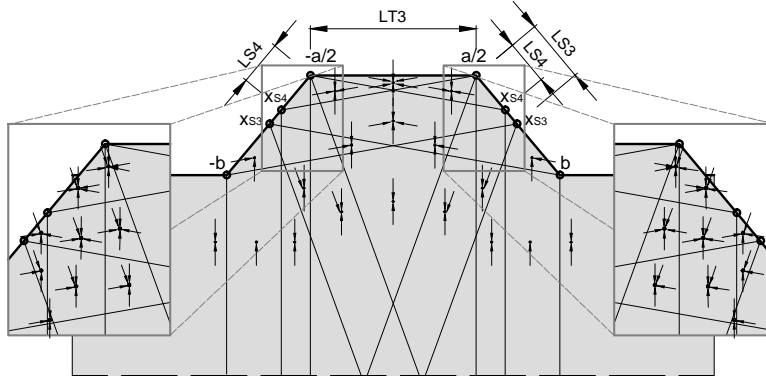


Figure 10: Propagation pattern associated to the optical field in a hill of aspect ratio  $a/h = 1.67$  and slope angle  $\beta = 50^\circ$ . The segments marked as  $L_{S3}$ ,  $L_{S4}$  and  $L_{T3}$  represent zones illuminated by the main incident system and by contributions from the slopes. Over these segments bounding values of the amplitude function can be predicted.

Two additional similar regions or concentration segments can be identified over the sloped part of the hill, labeled  $L_{S3}$  and  $L_{S4}$  in fig. 10. These segments are also illuminated by the main incident front and by reflected rays originated at the crest and at the opposite slope. The lengths and locations of the involved segments can be shown to be:

$$\begin{aligned}
 L_{T3} &= a \\
 L_{S3} &= \sqrt{(x_{S3} - (-a/2))^2 + (y_{S3} - (-h))^2} \\
 L_{S4} &= \sqrt{(x_{S4} - (-a/2))^2 + (y_{S4} - (-h))^2}
 \end{aligned}$$

where

$$\begin{aligned}
x_{S3} &= \frac{b(m_\phi + m_{LS})}{m_\phi - m_{LS}} \\
y_{S3} &= m_{LS}(x_{S4} + b) \\
x_{S4} &= \frac{m_\phi(a/2) - m_{LS}b - h}{(m_{LS} + m_\phi)} \\
m_\phi &= -\tan(\pi/2 - 2\beta) \\
m_{LS} &= -\tan(\beta).
\end{aligned}$$

In order to identify the fingerprint of the concentration segments introduced by the optical field we obtained an amplitude contour map or  $f - x$  diagram displaying the displacement amplitude over the normalized free surface against dimensionless frequency. Bounding values of 6.0 and 2.0 at the midpoint corresponding to constructive and destructive interference of the illuminating rays are clearly identified. Similarly, amplitude values oscillating between 0.0 and 4.0 are evident over the sloped parts of the hill marked by the segments  $L_{S3}$  and  $L_{S4}$ .

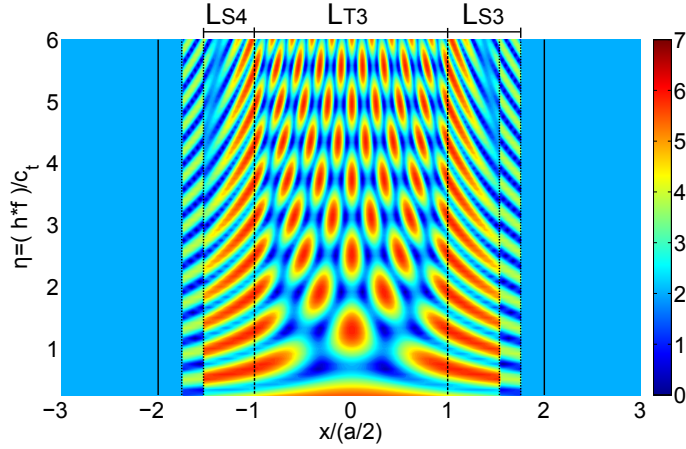


Figure 11: TFs for the optical field of a trapezoidal hill of aspect ratio  $a/h = 1.67$  and  $\beta = 50^\circ$ , where  $\beta > \pi/4$  and  $\alpha > (\pi - 2\beta)$

The geometric parameters used in the hill of fig. 10 correspond to a scenario where all the free surfaces (i.e., crest and slopes) interact with each other generating a relatively complex incoming field. In this work we were able to identify 5 geometrical scenarios, represented in terms of concentration segments and comprising all the possible scenarios for vertically incident waves. These are shown in table 1.

As has already been remarked, the geometric parameter controlling the complexity of the propagation pattern corresponds to the internal angle  $\alpha$  which fixes the location of the incidence and reflection boundaries. This result has as a main implication the fact that the level of complexity in the propagation pattern related to the optical field is not necessarily related to the level of complexity in the topographic features of the hill. This result is evident from the diagrams in table 1 where we show the boundaries and concentration segments for each one of the 5 scenarios.

In order to identify the difference in the propagation patterns associated to the optical field, we conducted time domain analysis for the hills belonging to each one of the 5 cases reported in table 1. To that end we used a Ricker pulse of central frequency  $f_c = 1.0Hz$  defined according to eq. (14). All the hills have an aspect ratio  $a/h = 1.67$  while the

slope angles are  $\beta = [30^0, 70^0, 40^0, 60^0, 50^0]$ . Figure 12 and fig. 13 show snapshots of the propagation patterns at different time instants. In the case of fig. 12 we have arranged the hills according to the level of complexity in the propagation pattern, while in fig. 13 the results have been arranged from gentle to strong slope.

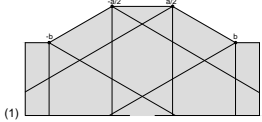
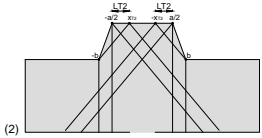
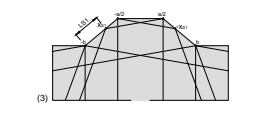
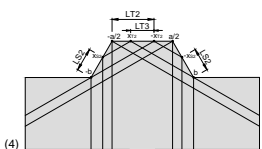
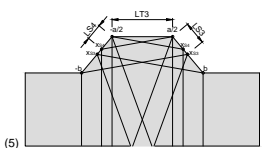
Pattern	$\beta$	$\alpha$	Notes	Ray diagram
1	$< \pi/4$	$< 2\beta$		(1) 
2	$> \pi/4$	$< (\pi - 2\beta)$	$b > h/\tan(2\beta - \pi/2)$	(2) 
			$b = a/2 + h/\tan\beta$	
			$L_{T2} = \sqrt{(x_{T2} - a/2)^2}$	
			$x_{T2} = \frac{-h+m_\phi b}{m_\phi}$	
			$y_{T2} = -h$	
3	$< \pi/4$	$> 2\beta$	$L_{S1} = \sqrt{(x_{S1} - b)^2 + (y_{S1})^2}$	(3) 
			$x_{S1} = \frac{h-m_\phi+m_{LS}b}{(m_\phi+m_{LS})}$	
			$y_{S1} = -m_{LS}(x_{S1} - b)$	
			$m_{LS} = -\tan(\beta)$	
4	$> \pi/4$	$< (\pi - 2\beta)$	$b < h/\tan(2\beta - \pi/2)$	(4) 
			$L_{S2} = \sqrt{(-b - x_{S2})^2 + (y_{S2})^2}$	
			$x_{S2} = \frac{m_\phi x_{T2} - h - m_{LS}b}{(m_{LS} + m_\phi)}$	
			$y_{S2} = m_{LS}(x_{S2} + b)$	
			$L_{T2} = \sqrt{(x_{T2} - a/2)^2}$	
			$x_{T2} = \frac{-h+m_\phi b}{m_\phi}$	
			$y_{T2} = -h$	
$L_{T3} = 2L_{T2} - a$				
5	$> \pi/4$	$> (\pi - 2\beta)$	$L_{T3} = a$	(5) 
			$L_{S3} = \sqrt{(x_{S3} - (-a/2))^2 + (y_{S3} - (-h))^2}$	
			$x_{S3} = \frac{b(m_\phi+m_{LS})}{m_\phi-m_{LS}}$	
			$y_{S3} = m_{LS}(x_{S3} + b)$	
			$L_{S4} = \sqrt{(x_{S4} - (-a/2))^2 + (y_{S4} - (-h))^2}$	
$x_{S4} = \frac{m_\phi(a/2)-m_{LS}b-h}{(m_{LS}+m_\phi)}$				

Table 1: Propagation pattern associated to the optical field. Pattern (1) corresponds to a simple pattern while pattern (5) represents a high level of interaction or a complex propagation pattern

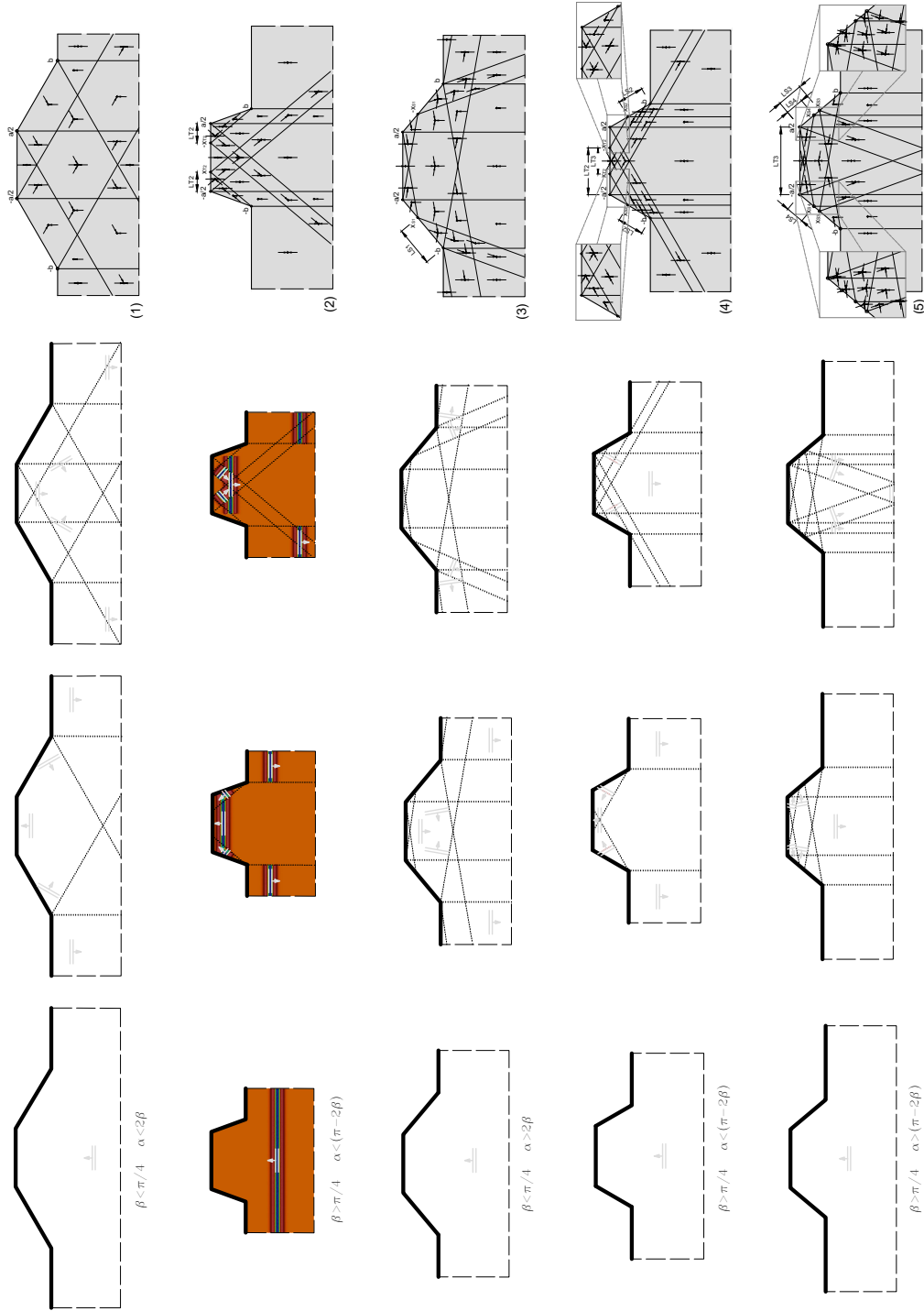


Figure 12: Snapshots of the propagation patterns at different time instants arranged according to the lower to higher complexity in the propagation pattern, for a hill with aspect ratio  $a/h = 1, 67$



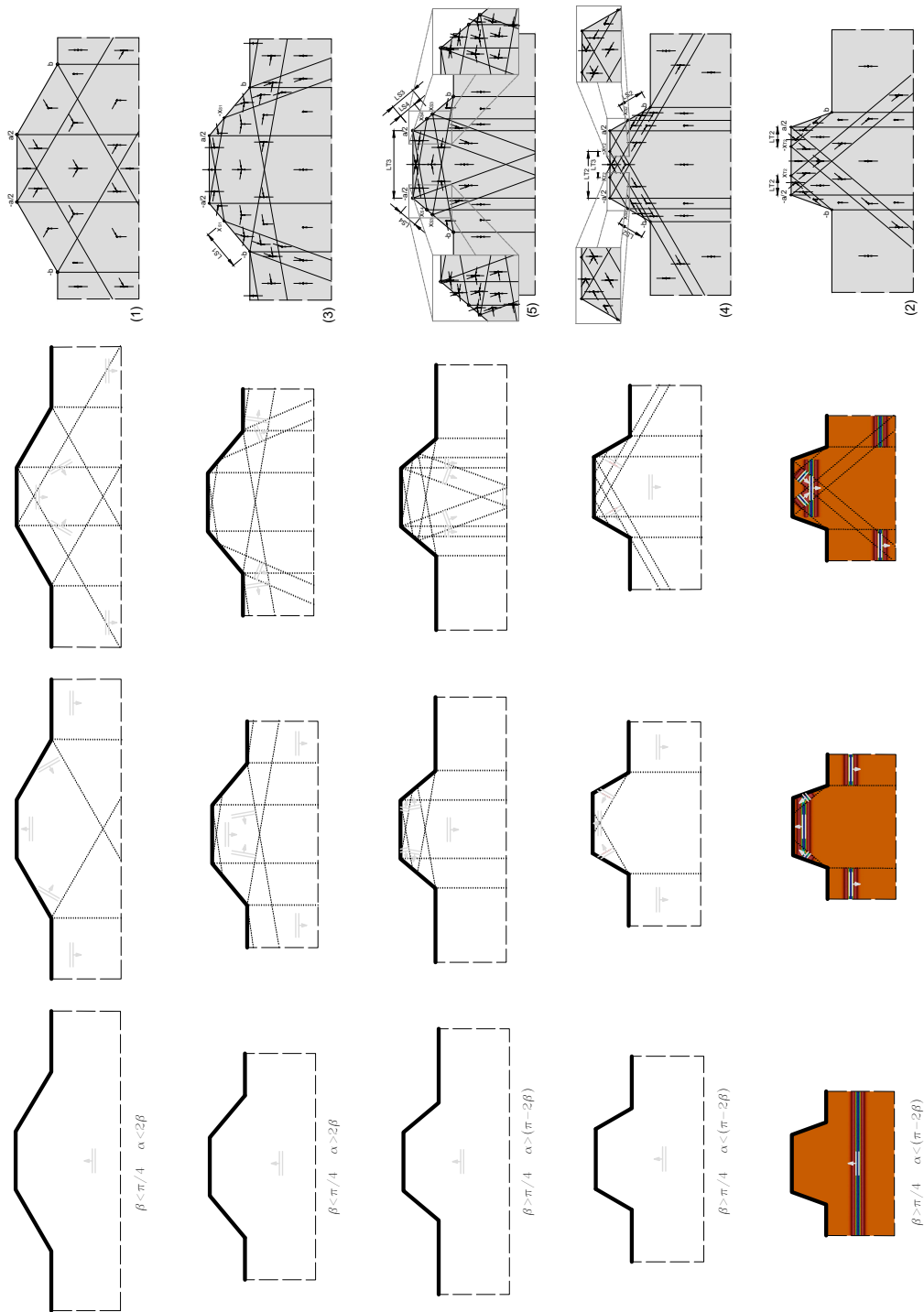


Figure 13: Snapshots of the propagation patterns at different time instants arranged from gentle to strong slope, for a hill with aspect ratio  $a/h = 1, 67$

In addition to the snapshots for the different scenarios described previously we have also plotted the contour maps for the transfer functions shown in fig. 14. These maps allows us to identify the level of complexity and its spatial variation with frequency for the different concentration segments. From these TFs it is observed that the so called levels of complexity defined herein in terms of concentration segments are frequency independent. Moreover, the only difference in these TFs is the stronger spatial variation as the frequency increases.

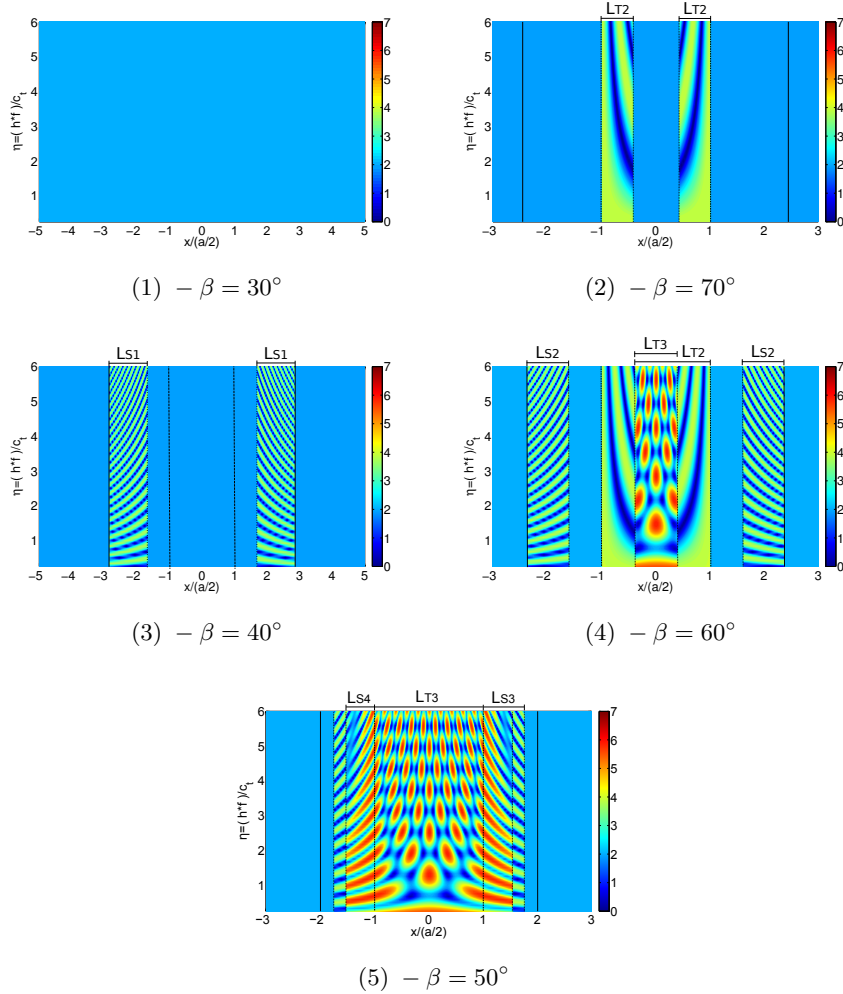


Figure 14: TFs for the optical field of a trapezoidal hill of aspect ratio  $a/h = 1.67$  and  $\beta = 50^\circ$  for the 5 propagation patterns, arranged according to its complexity.

For a hill of a given aspect ratio  $a/h$ , it is possible to obtain results with propagation patterns pertaining to each one of the 5 possible scenarios depending on the slope angle  $\beta$ . For instance fig. 15, corresponding to a hill with a ratio  $a/h = 0.25$ , shows the variation of the concentration segments as a fraction of the crest width for different values of the slope angle. In particular we identify pattern (1) for  $\beta < 31^\circ$ , pattern (3) for  $31^\circ < \beta < 45^\circ$  and pattern (5) for  $45^\circ < \beta < 77^\circ$ .

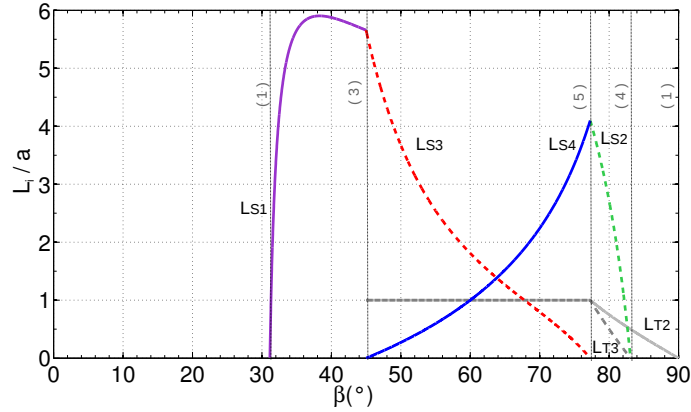


Figure 15: Range of variation of the different concentration segments with the slope angle for a hill with aspect ratio  $a/h = 0.25$

The variation in the concentration segments for different values of the aspect ratio are shown in fig. 16. It is clear how the lengths of these segments approaches zero as the hill becomes flat. On the other hand it can be observed that patterns (1) and (2) correspond to lower and upper bounds of the slope angle, indicating once again that the level of complexity of the propagation pattern is not directly connected to the value of the slope angle. This is evident from the intermediate range of angles where we can identify patterns 3, 4 and 5, which becomes smaller as the aspect ratio increases. This behavior indicates that in very wide hills there is a reduced set of values of the slope angles leading to complex propagation patterns.

For comparison these plots are reproduced again in fig. 17 where the scale has been modified in order to identify the variation of each involved zone even in the case of very flat hills.

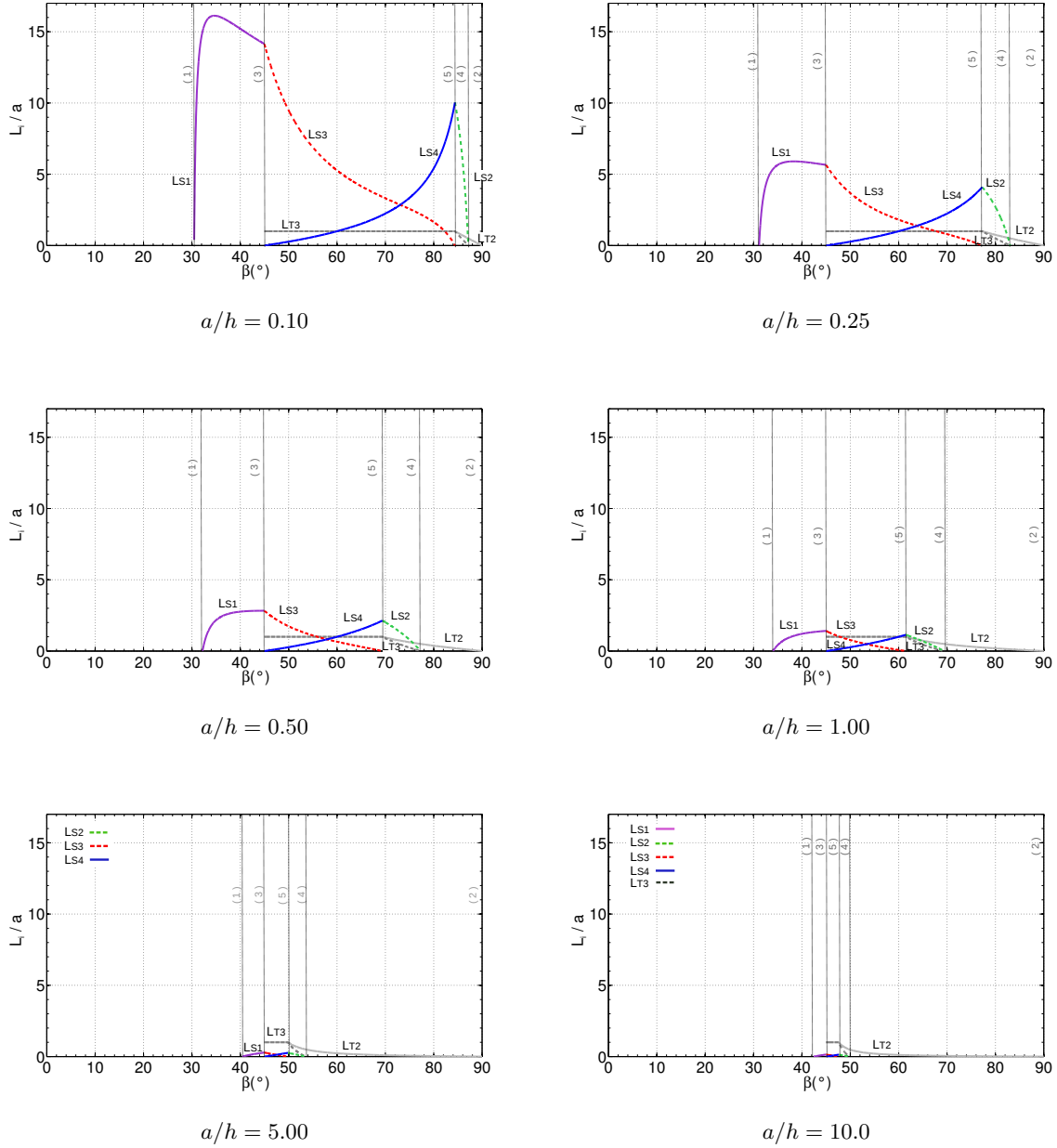


Figure 16: Concentration segments variation,  $L_{S1}$ ,  $L_{S2}$ ,  $L_{S3}$ ,  $L_{S4}$ ,  $L_{T2}$  and  $L_{T3}$ , according to the slope inclination  $\beta$ .

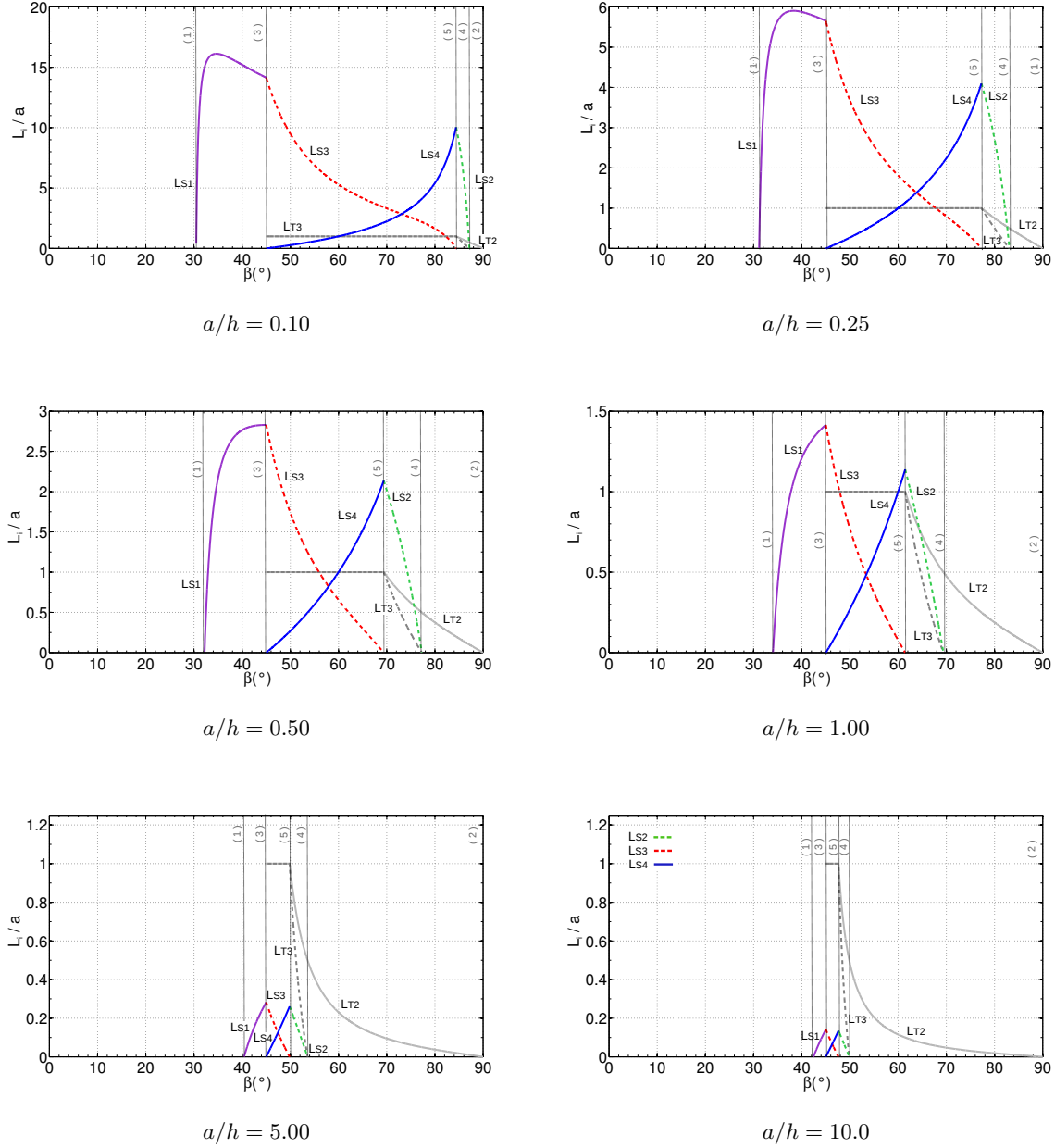


Figure 17: Concentration segments variation,  $L_{S1}$ ,  $L_{S2}$ ,  $L_{S3}$ ,  $L_{S4}$ ,  $L_{T2}$  and  $L_{T3}$ , according to the slope inclination  $\beta$  - Modified scale.

### 3.2.1 Total solution

The total solution is now examined by separating the optical and diffracted fields. Regarding the optical field, it has been shown that a relatively simple geometric analysis yielded 5 controlling propagation patterns providing the analyst with a great deal of control over this specific part of the solution. An equivalent understanding of the diffracted component would allow us to identify which part of the solution prevails in a given scenario. However, the contribution from the diffracted field is complicated as it depends on many different parameters like, the number of originating sources; its frequency dependent nature; and

most important, the fact that it involves an infinite number of terms of varying amplitude. As a result, a geometric analysis analogous to the one adopted for the optical field is not possible. However, if we use some of the fundamental concepts pertaining to the superposition based diffraction technique, in combination with the 5 optical propagation patterns we are able to identify some effects over the total solution that are in fact caused by the diffracted part of the motion.

The diffracted field possesses the strong property of restoring continuity along the reflection and incidence boundaries of the optical field. This is illustrated in fig. 18 where we show the first order diffraction generated over the right top wedge, for two hills of aspect ratio  $a/h = 1.0$  and slope angles of  $\beta = 42^\circ$  and  $\beta = 35^\circ$  respectively. It is observed how the diffraction boundary is closest to the surface for the higher value of slope angle.

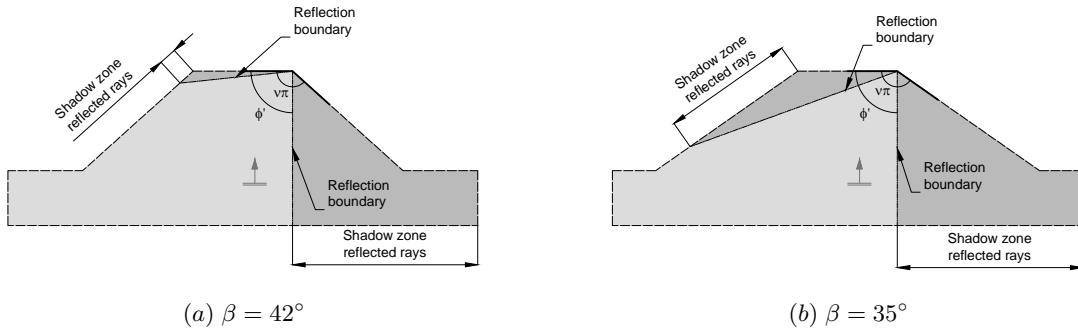


Figure 18: Location of the diffraction boundaries of a trapezoidal hill with aspect ratio  $a/h = 1.00$ .

A similar observation can be made in the case shown in fig. 19 where we now describe the variation of the diffraction boundaries for two hills of aspect ratio  $a/h = 1.67$  and slope angles  $\beta = 30^\circ$  and  $\beta = 40^\circ$ , corresponding to propagation patterns 1 and 3 respectively. In the  $\beta = 40^\circ$  slope there is a discontinuity in the diffraction term corresponding to the reflection of a first-order diffraction, which was necessary in order to restore continuity of the second reflection of the incident wave in the slope over the right hand side of the hill. This discontinuity is not present in the  $\beta = 30^\circ$  slope.

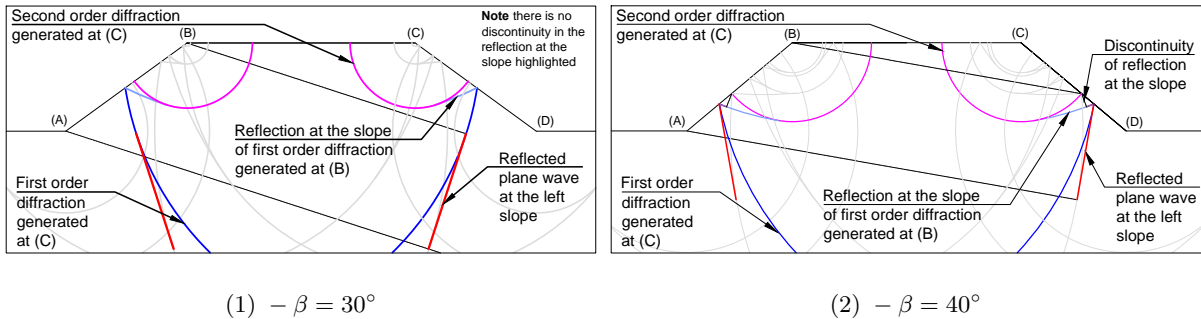


Figure 19: Variation of the diffraction boundaries for two hills of aspect ratio  $a/h = 1.67$  and slope angles  $\beta = 30^\circ$  and  $\beta = 40^\circ$ , adjusting to the discontinuities of the optical field.

From the above two cases it is clear that the diffraction boundaries undergo changes from one particular geometry to the other. These variations in the diffraction field not only contribute to restoring continuity in the optical field, but most important, these diffracted

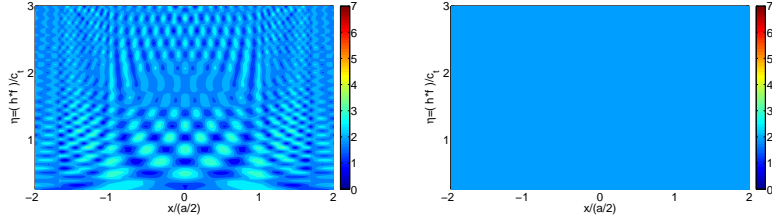
terms have the strong property of keeping smooth the transition among the geometries encompassed by the 5 propagation patterns after counteracting the effect of the optical field. As a consequence, if the ranges of existence of the different propagation patterns are close to each other, the diffraction term will control the total solution weakening the contribution from the optical field. By contrast, if these ranges are separated, the solution is controlled by the optical field.

As concluded from the observations in relation to fig. 17, the ranges of existence of the different propagation patterns become smaller as the aspect ratio  $a/h$  increases. If we connect this idea with the smoothing effect of the diffraction field near these limits, one should expect that at these  $a/h$  ratios the contribution from the optical field was weak and the response is mainly controlled by the diffracted field.

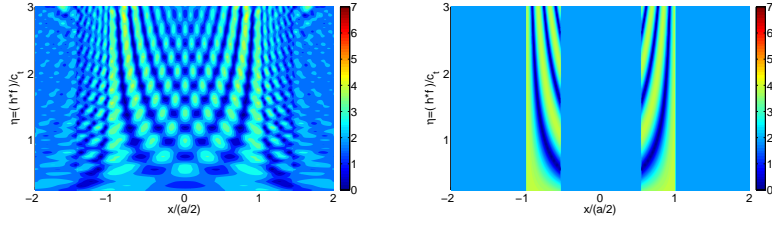
In fig. 20 and fig. 21 we show a comparison between the transfer functions for the total solution and the optical field for hills of aspect ratios  $a/h = 5.0$  and  $a/h = 1.0$  respectively. In the first case (i.e.,  $a/h = 5.0$ ), the differences in the transfer functions from one pattern to the other are almost negligible. There are only a small differences in amplitude located precisely over the concentration segments of the optical field. For instance, this is clearly observed in pattern (2) corresponding to  $\beta = 60^\circ$  where there is an increase in amplitude over a segment identified as ( $L_{T2}$ ).

For smaller aspect ratios, and particularly for those cases in which the range of slope angles associated to each pattern are largely separated from each other, the transfer functions exhibit differences from one propagation pattern to the other. Moreover, the similarities between the total solution and the optical field are evident and clearly observed to be controlled by the concentration segments in the optical field. For instance, in the hills corresponding to the patterns (4) and (5) with slope angles of  $\beta = 65^\circ$  and  $\beta = 75^\circ$  respectively, the maximum amplitude in the total field approaches the value of 6.0 previously identified in the optical solution.

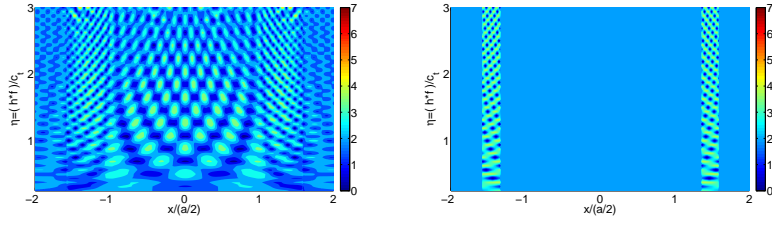
An additional observation from fig. 20 and fig. 21 is that in both cases the similarity between the total and optical fields is stronger in the high frequency range. This observation may be explained by the diffraction contribution, since in the lower frequencies the amplitude of the higher order diffracted fronts is stronger, resulting in an counteracting effect against the contribution from the optical field.



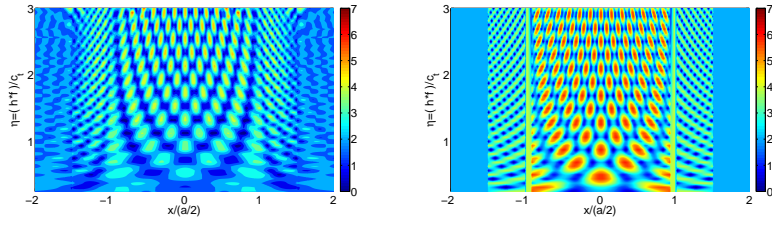
(1)  $-\beta = 35^\circ$



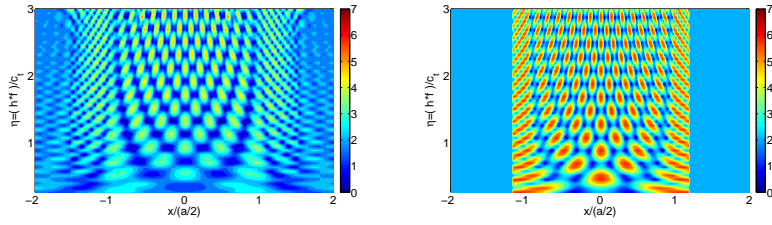
(2)  $-\beta = 60^\circ$



(3)  $-\beta = 42^\circ$



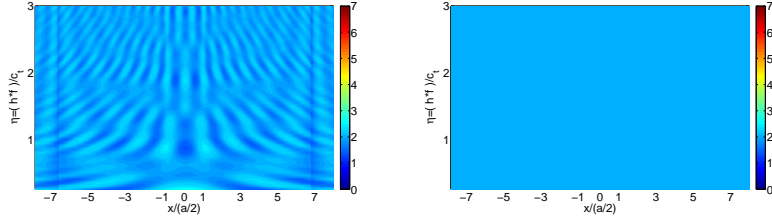
(4)  $-\beta = 50^\circ$



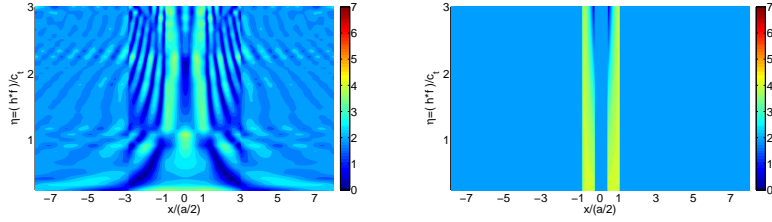
(5)  $-\beta = 48^\circ$

Figure 20: TFs for the total field (left) and optical field (right) for an aspect ratio  $a/h = 5.0$ , arranged according to the lower to higher complexity in the propagation pattern of the optical field.

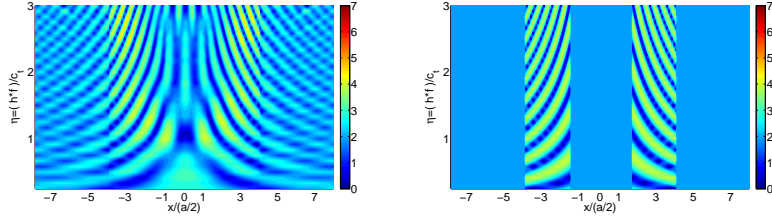




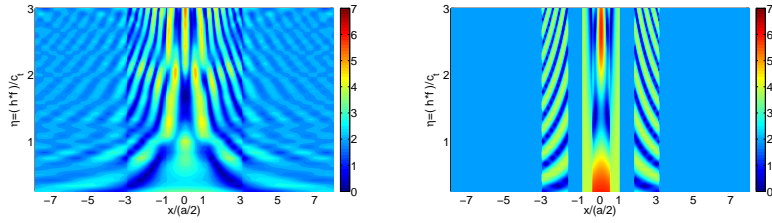
(1)  $-\beta = 20^\circ$



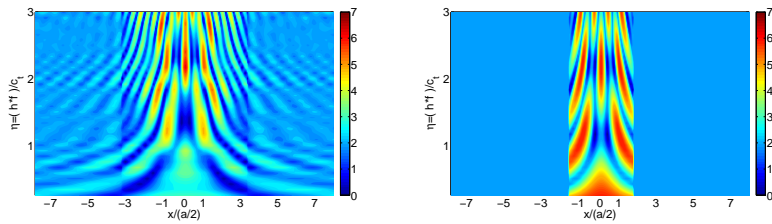
(2)  $-\beta = 75^\circ$



(3)  $-\beta = 40^\circ$



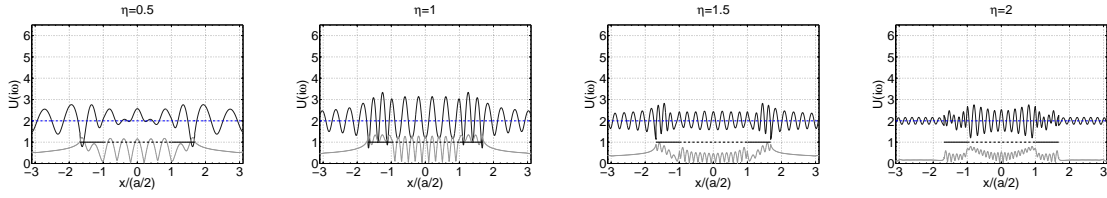
(4)  $-\beta = 65^\circ$



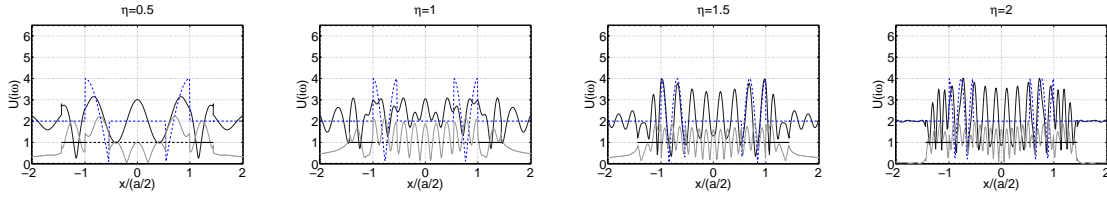
(5)  $-\beta = 55^\circ$

Figure 21: TFs for the total field (left) and optical field (right) for an aspect ratio  $a/h = 1.0$ , arranged according to the lower to higher complexity in the propagation pattern of the optical field.

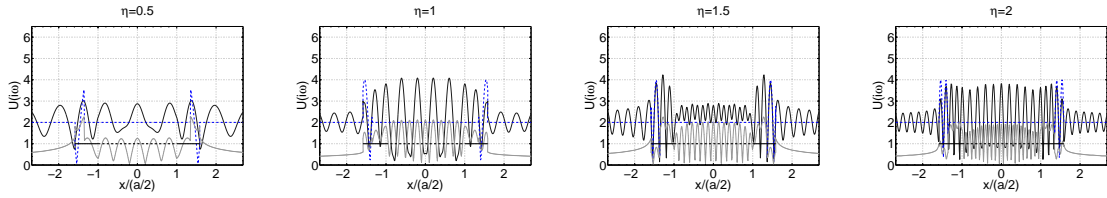
In fig. 22 we present the spatial distribution of the amplitude functions for hills corresponding to the 5 propagation patterns for 4 different values of the dimensionless frequency parameter  $\eta$ . In each case we show the independent contribution from the optical field (described by the dashed blue line) and diffracted field and its superposition in terms of the total solution (described by the continuous black line). It is observed that in the low frequency regime (e.g.,  $\eta = 0.5$  and  $\eta = 1.0$ ) the differences between the total and optical fields are stronger than in the high frequency regime ( $\eta = 1.5$  y  $\eta = 2.0$ ) confirming once again the de-amplification effect introduced by the diffraction contribution in the low frequency regime. This explains the fact that the optical field controls the solution at the high frequency regime. On the other hand, the diffracted field (shown by the gray continuous line) exhibits discontinuities that change from one propagation pattern to the other. For instance consider the cases corresponding to patterns (4) and (5) at the dimensionless frequency  $\eta = 0.5$ . In (4) there is only one discontinuity that extends from  $x/(a/2) = 1$  to  $x/(a/2) \approx 1.5$ , while over the same segment on pattern (5) there are two discontinuities. These discontinuities in the diffracted field produce a similar total field, even when there are important differences in the optical solution. A final observation regarding the contribution from the diffracted field is the fact that its contribution is highly relevant over the crest, where several diffraction sources interact with each other, while over the flat part of the half-space, this component of the response is moderate as it is produced by a single diffraction source.



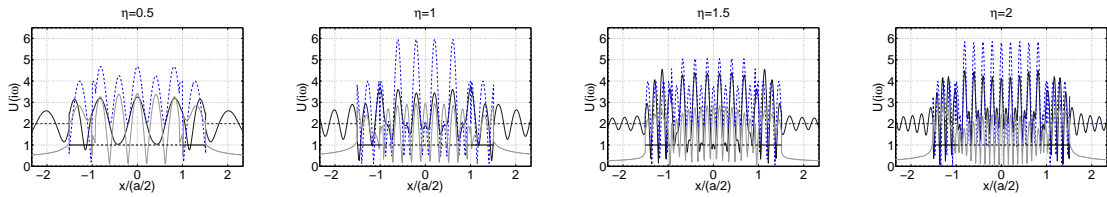
(1)  $-\beta = 35^\circ$



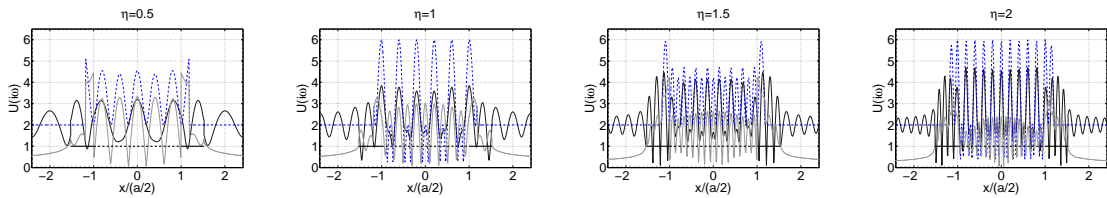
(2)  $-\beta = 60^\circ$



(3)  $-\beta = 42^\circ$



(4)  $-\beta = 50^\circ$



(5)  $-\beta = 48^\circ$

Figure 22: TFs along the surface for dimensionless frequencies  $\eta = [0.25, 0.50, 1.0, 1.5]$  and aspect ratio  $a/h = 5.0$ , where the total field is black continuous line, the optical field is the dashed blue line and the diffracted field the gray continuous line, arranged according to the lower to higher complexity in the propagation pattern of the optical field..

In some cases the diffracted field has the ability to counteract the optical solution to the extent that this component is hardly observable. This scenario arises in the following cases:

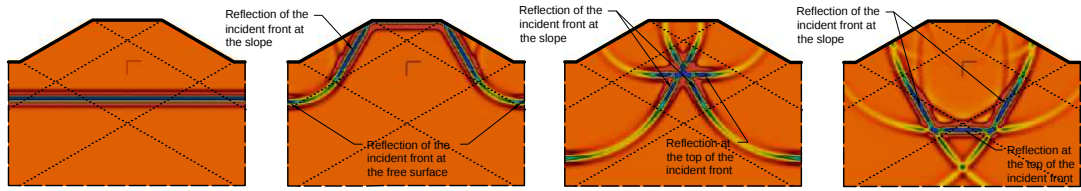
- When the geometry corresponds to a limit propagation pattern and the hill has a high aspect ratio  $a/h$ .
- At the low dimensionless frequency regime, where the higher order diffraction terms contribute with high amplitudes values thus making strong contribution to the total solution.

Under different scenarios, one finds that the contribution from the optical field is important and the general results for the identified propagation patterns is useful as a first order engineering approximation.

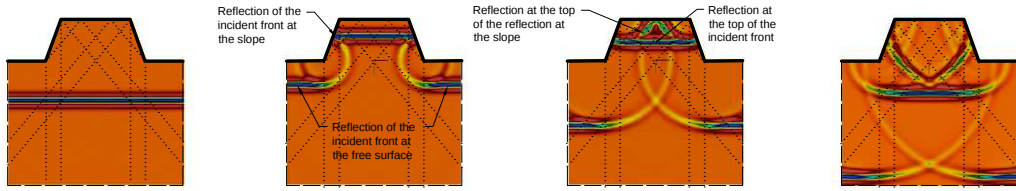
### 3.3 Time domain solution

The transfer functions, obtained from the frequency domain analysis are now used to synthesize time domain solutions via fast fourier transforms. Figure 23 displays snapshots at 4 time instants of the propagation patterns for a hill with aspect ratio  $a/h = 1.67$  and various slope angles. The cases considered correspond to the patterns and levels of complexity identified in the frequency domain analysis. For clarity the hills are drawn at the same scale. The optical and diffracted fields correspond to the plane and cylindrical fronts respectively.

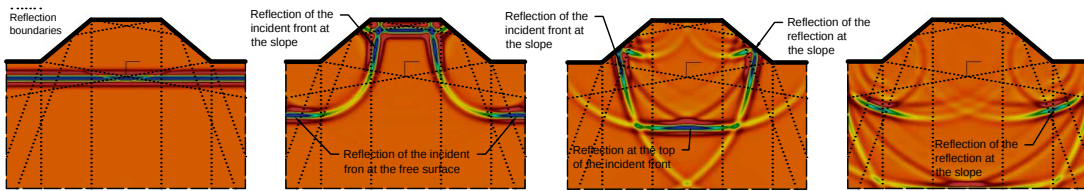
From the time domain solution it becomes evident how the diffracted field smooths out the discontinuities in the optical solution. On the other hand, concentration segments (where several rays converge) are enclosed by the reflection boundaries marked by the dashed lines extending over the domain. The snapshots corresponding to the first time instant (column 1) display the incident field before hitting the slope. The second set of snapshots show the first diffracted waves generated by the interaction of the incident fronts with the bottom sources. Similarly, the third and fourth snapshots depict the diffracted waves generated by the upper sources and also the higher order diffractions produced by secondary events. These higher order terms produce motions of increased duration as energy becomes trapped between adjacent sources of diffraction. Since this part of the field attenuates with distance, its effect is expected to be less important for hills with extended crests (i.e., large aspect ratios). The diffracted field may also have important effects on the final amplitude according to the type of interference with the optical field. Finally, it is observed that the diffracted field completes or restores the reflected front in order to recover radiation boundary conditions over the far field. To complete the time domain analysis we also show in fig. 24 synthetic seismograms over the surface of the different hills. In particular, these seismograms show the energy trapping effect produced by adjacent diffraction sources and responsible for the increase in duration over the hill.



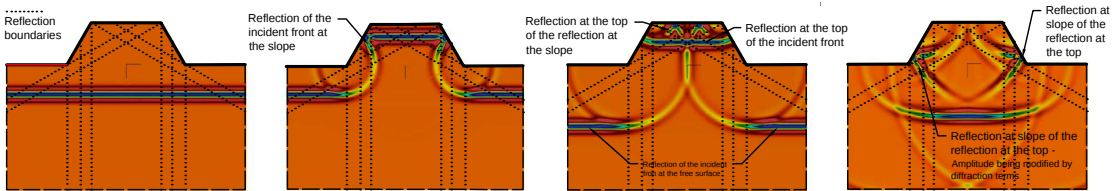
(1)  $-\beta = 30^\circ$



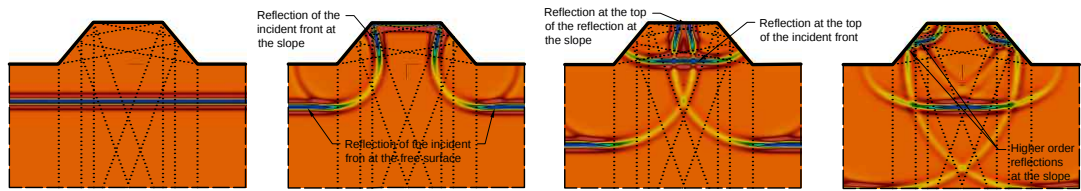
(2)  $-\beta = 70^\circ$



(3)  $-\beta = 40^\circ$



(4)  $-\beta = 60^\circ$



(5)  $-\beta = 50^\circ$

Figure 23: Snapshots of total displacement field at different time instants, arranged according to the lower to higher complexity in the propagation pattern of the optical field, for a hill with aspect ratio  $a/h = 1,67$

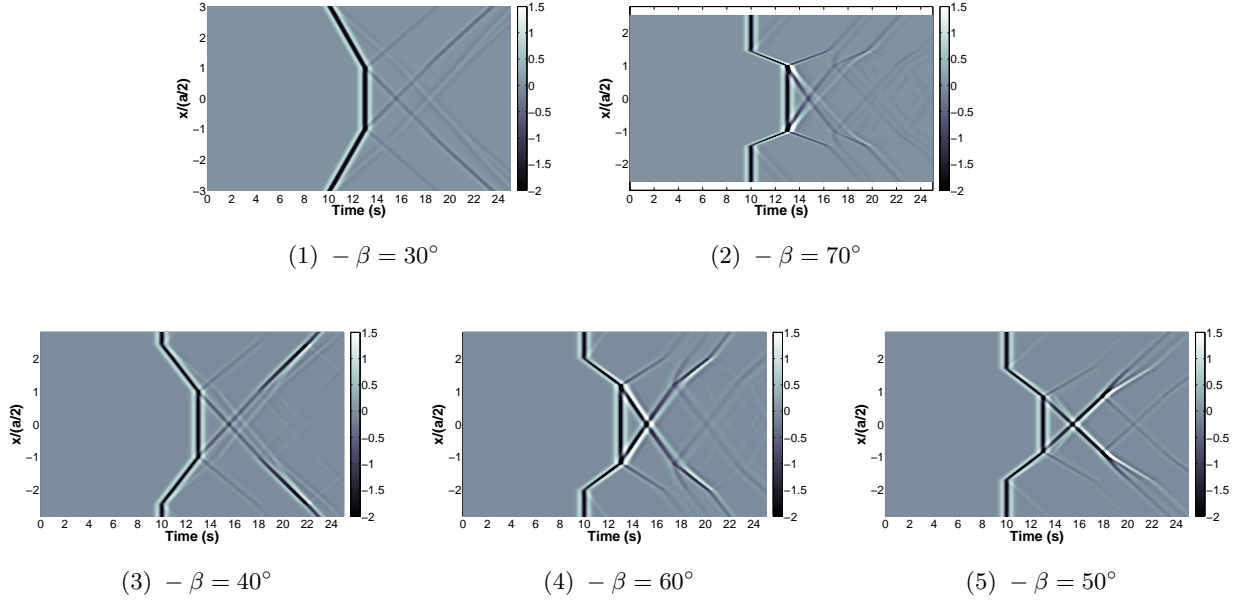


Figure 24: Synthetic seismograms (displacements) at the surface of a trapezoidal hill with  $a = 1.67h$ .

We also computed response spectra for 5 hills of aspect ratio  $a/h = 1.0$  and various slope inclinations. Once again, the 5 considered scenarios represent the 5 possible propagation patterns previously identified. For each hill the response was obtained at the toe; at the mid-slope and in the center of the crest. Figure 25 shows the acceleration time history and the corresponding Fourier spectra used as free field motion. We selected a signal with frequency content similar to the one contained in the transfer functions for the studied hills. The resulting time histories and corresponding response spectra for the 5 hills and considered points are shown in fig. 26. In the figures the dashed gray lines correspond the response spectra for the free-field. For completeness we also obtained ratios of response spectra (RRS) between the solution at the different points over the slope and the free-field motion. These RRSs can be used as empirical transfer functions used to obtain the response spectra for points over the hill given the response spectra compatible with the free field motion. From the computed spectra it is clear that for the 5 scenarios and the three considered points there is a period lengthening with respect to the free field motion. The largest period difference occurs at points over the mid-slope (see patterns 4 and 5 in fig. 26). The fact that this lengthening effect is independent of the geometric level of complexity existing in the optical field implies that the period shifting is completely due to the diffraction field. On the other hand, larger amplifications are observed over the crest. This amplification is stronger as the complexity in the optical field increases, which suggests that while the period shifting is controlled by the diffraction field, the amplification value is controlled by the optical field.

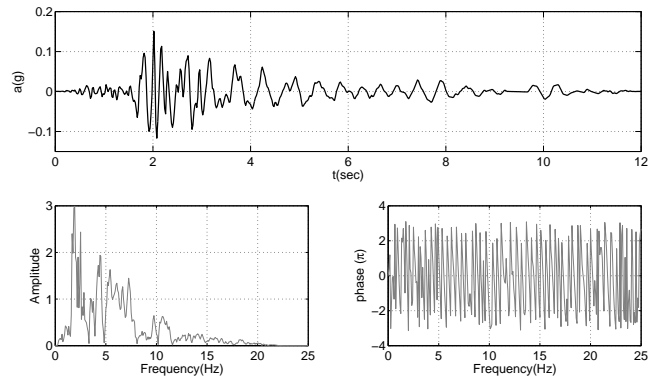
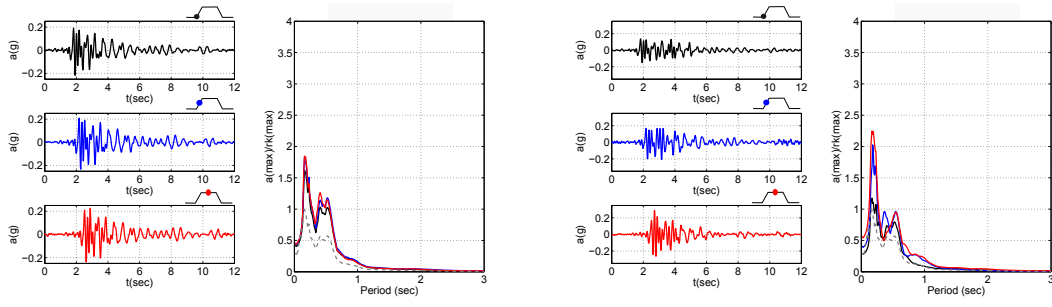
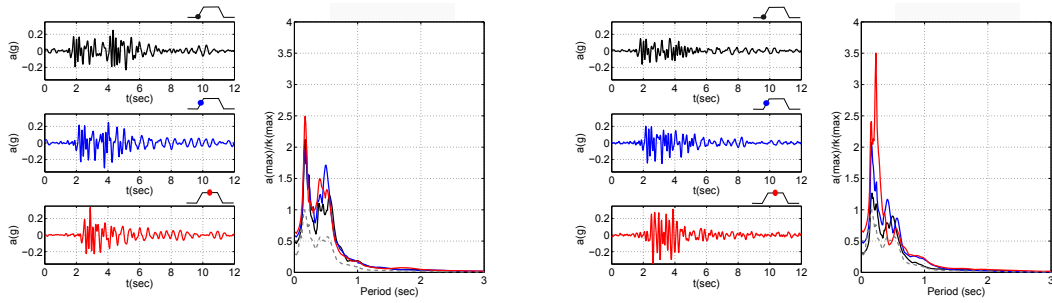


Figure 25: Free field motion acceleration time history and its corresponding Fourier spectra



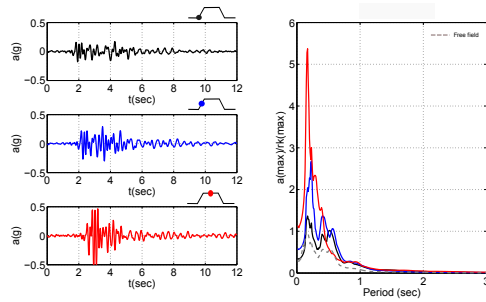
(1)  $-\beta = 20^\circ$

(2)  $-\beta = 75^\circ$



(3)  $-\beta = 40^\circ$

(4)  $-\beta = 65^\circ$



(5)  $-\beta = 55^\circ$

Figure 26: Response spectra normalized with respect to the peak spectra acceleration of the free field motion of a hill with aspect ratio  $a/h = 1.0$  at three point along the surface: toe of the slope (black); at the mid-slope (blue) and in the center of the crest (red).



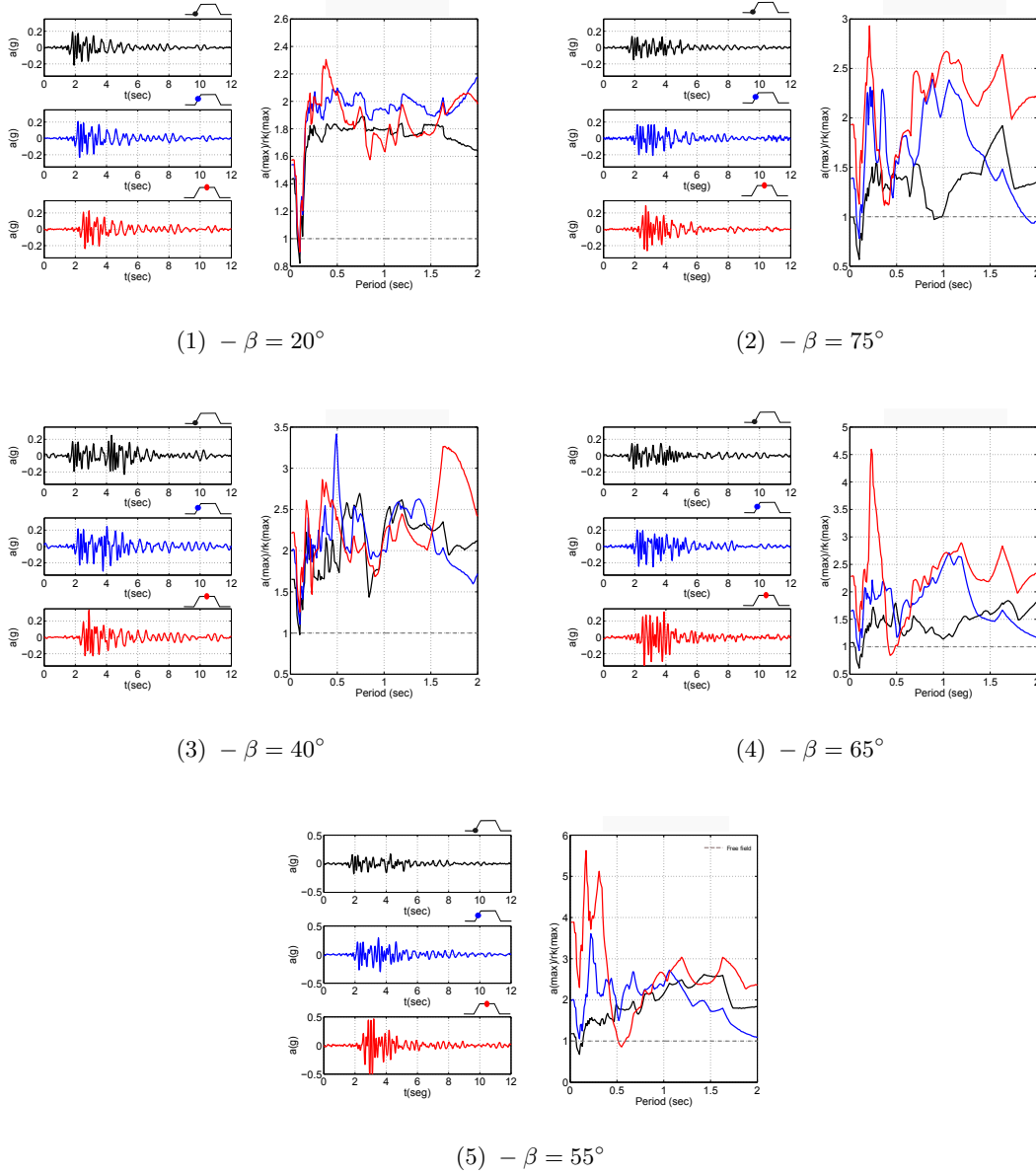


Figure 27: Ratios of response spectra (RRS) between the solution at the different points over the slope and the free-field motion of a hill with aspect ratio  $a/h = 1.0$ , at three point along the surface: toe of the slope (black); at the mid-slope (blue) and in the center of the crest (red).

## 4 Conclusions

We have studied the frequency domain response of trapezoidal hills submitted to vertically incident  $SH$  waves. The study was conducted from a geometric point of view with the aim of identifying the dependency of the response on the main geometric features of the hill and therefore its subsequent influence on topographic effects in earthquake engineering. For that purpose we first solved the problem using a boundary element based numerical algorithm. The total solution was then analysed using a method reported in the literature

which splits the field into the contribution of the incident waves and its reflections (i.e., the optical field), and a contribution due to the sources of diffraction. In the method, the diffracted part of the response is formulated as a fundamental solution for an infinite wedge. From the basic knowledge of this last term, and in particular from its frequency dependent nature, it is evident that at higher frequencies the solution is expected to be controlled by the optical field while at the low frequency range the diffracted field takes over. From the point of view of the optical field, we were able to find 5 possible propagation patterns encompassing every possible geometric scenario. These patterns differ from each other on the level of interaction of the incoming rays with the free surfaces of the hill. In these work such patterns have been labelled as complexity levels. We provide expressions to predict limits of the amplitude function and location over the hill surface in each one of the scenarios. Furthermore, from these analyses we found that the slope angle  $\beta$  does not necessarily controls the complexity in the response, and surprisingly gentle slopes with a given combination of geometric parameters may exhibit stronger propagation patterns than those of a steep slope. The range of angular values for which the propagation patterns of increased complexity arise are relatively short and the range decreases in the direction of increasing aspect ratio  $a/h$ .

From the point of view of the diffracted field, it was found that this part of the response carries with it boundaries which are coincident with those existing in the optical field and demarcating shadow and illuminated zones. These boundaries provide a smooth transition among the 5 scenarios identified from the optical solution. As a result the diffracted field is stronger when the angular ranges of the complex patterns are reduced. This behaviour implies that at low values of the dimensionless frequency  $\eta$  and high aspect ratios  $a/h$  the solution is controlled by the optical field and a geometric solution can be used as a first order approximation.

Finally, the spectral response showed that the hill has the effect of lengthening the period obtained from the incident motion and an amplification effect which is strongly tied to the level in complexity of the optical field. It is thus found that while the optical field controls the topographic amplification, the diffracted field controls the fundamental site period.

## 5 Acknowledgments

This project was conducted with financial support of Eafit University. Also, thanks to Prof. Juan Gomez, Prof. Juan Jaramillo and Grupo de Investigación en Mecánica Aplicada of Universidad EAFIT for its contribution and support throughout the course of this project.

## 6 Appendix

The optical field in the studied scenarios was computed with an in-house computer code (*Rays*). The code allows one to find the frequency domain solution for points along the boundary and inside a predefined computational domain. The code also computes the time domain response for a given input time series. The code is organized as follows:

1. Reads the input model given in terms of geometric parameters of the hill, definition of the input signal and location of points for output.
2. Computation of the frequency domain transfer function for each frequency and observation point.
3. Computation of the time domain response for every observation point.
4. Post-processing. Generation of time series of the response for visualization in third-party software. The following output files are generated:
  - Real and imaginary component of the transfer function.
  - Output file (extension `.vtk`) to be read by the third-party visualization software **ParaView**.

By default, the code (*Rays*) uses as input time series a Ricker pulse of characteristic frequency  $f_c$ , central time  $t_{ini}$  and total time  $t_{final}$  which is directly defined within the code. The code also requires definition of the shear wave propagation velocity  $c_t$  and density  $\rho$  of the medium (by default values correspond to  $f_c = 1Hz$ ,  $c_t = 1.0km/s$  y  $\rho = 1000kg/m^3$ ). The geometric parameters of the trapezoidal hill are: width  $a$  [km], slope angle  $\beta$  [°] and height  $h$  [km]. These properties are input in a file named `casoij.txt` as shown in the following example for specific values  $a = 1km$ ,  $\beta = 20^\circ$  and  $h = 1km$

```
1 | 1.0 20 1.0
```

The code uses the third-party mesher **Gmsh** to create observation points over the surface and inside the computational domain. The mesher generates the file `rays_sln.msh`. The pseudocode is shown in fig. 28.

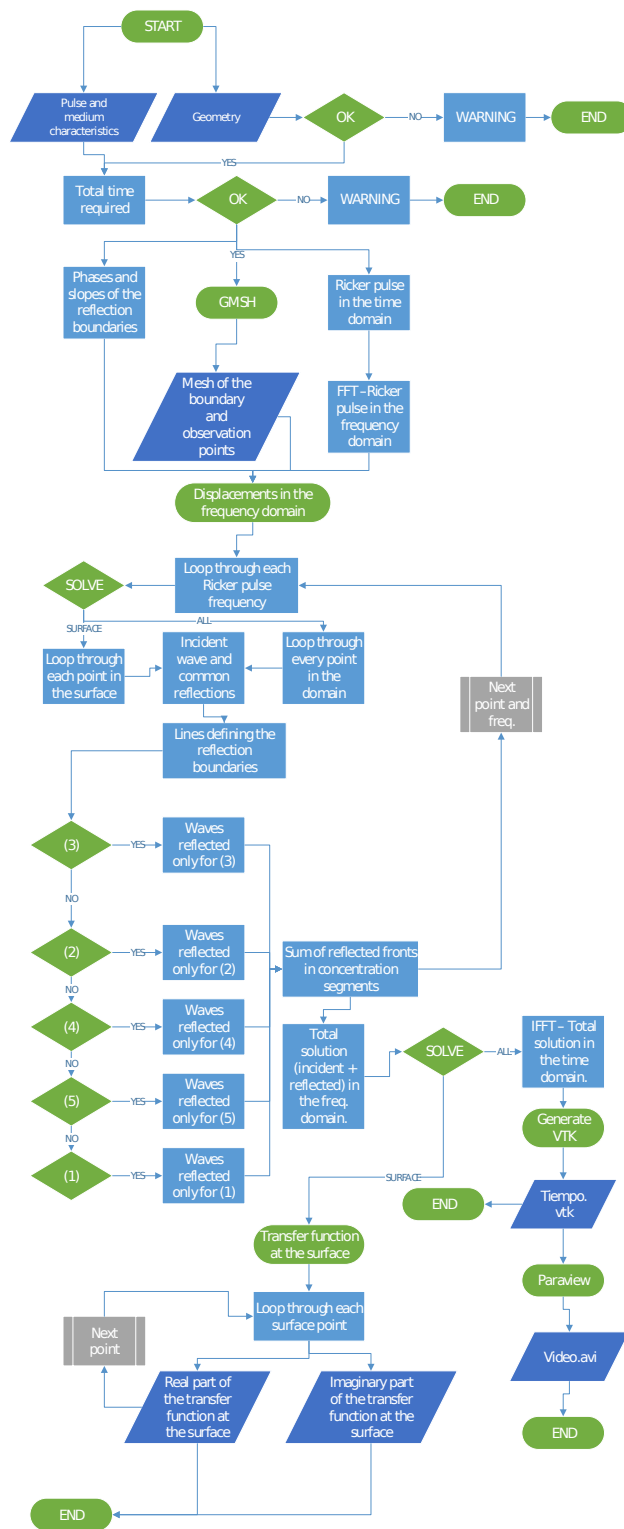


Figure 28: Flowchart of the code *Rays* used to compute the optical solution.

## References

- Amelsakhi, M., Sohrabi-Bidar, A., & Shareghi, A., 2014. Spectral assessing of topographic effects on seismic behavior of trapezoidal hill, *International Journal of Environmental, Earth Science and Engineering*, **8**.
- Ashford, S. A., Sitar, N., Lysmer, J., & Deng, N., 1997. Topographic effects on the seismic response of steep slopes, *Bulletin of the Seismological Society of America*, **87**(3), 701–709.
- Assimaki, D., Gazetas, G., & Kausel, E., 2005. Effects of local soil conditions on the topographic aggravation of seismic motion: parametric investigation and recorded field evidence from the 1999 athens earthquake, *Bulletin of the Seismological Society of America*, **95**(3), 1059–1089.
- Banerjee, P. K. & Butterfield, R., 1981. *Boundary element methods in engineering science*, vol. 17, McGraw-Hill London.
- Bard, P.-Y., 1997. Local effects on strong ground motion: basic physical phenomena and estimation methods for microzoning studies, *SERINA—Seismic Risk: An Integrated Seismological, Geotechnical and Structural Approach*, pp. 229–299.
- Furumura, T. & Koketsu, K., 1998. Specific distribution of ground motion during the 1995 kobe earthquake and its generation mechanism, *Geophysical Research Letters*, **25**(6), 785–788.
- Gelagoti, F., Kourkoulis, R., Anastasopoulos, I., & Gazetas, G., 2012. Nonlinear dimensional analysis of trapezoidal valleys subjected to vertically propagating sv waves, *Bulletin of the Seismological Society of America*, **102**(3), 999–1017.
- Gomez, J., Restrepo, D., Jaramillo, J., & Valencia, C., 2013. Analysis of the role of diffraction in topographic site effects using boundary element techniques, *Earthquake Science*, **26**(5), 341–350.
- Jaramillo, J., Gomez, J., Saenz, M., & Vergara, J., 2012. Analytic approximation to the scattering of antiplane shear waves by free surfaces of arbitrary shape via superposition of incident, reflected and diffracted rays, *Geophysical Journal International*, p. ggs061.
- Jaramillo, J. D., 2014. Damian bem sh: Boundary element based code for the analysis of scattering problems under plane sh waves, Personal communication. Universidad EAFIT. Applied Mechanics Group.
- Kaiser, A., Holden, C., Beavan, J., Beetham, D., Benites, R., Celentano, A., Collett, D., Cousins, J., Cubrinovski, M., Dellow, G., et al., 2012. The mw 6.2 christchurch earthquake of february 2011: preliminary report, *New Zealand journal of geology and geophysics*, **55**(1), 67–90.
- Kamalian, M., Sohrabi-Bidar, A., Razmkhah, A., Taghavi, A., & Rahmani, I., 2008. Considerations on seismic microzonation in areas with two-dimensional hills, *Journal of earth system science*, **117**(2), 783–796.
- Kawase, H., 1996. The cause of the damage belt in kobe: “the basin-edge effect,” constructive interference of the direct s-wave with the basin-induced diffracted/rayleigh waves, *Seismological Research Letters*, **67**(5), 25–34.
- Kawase, H. & Aki, K., 1990. Topography effect at the critical sv-wave incidence: possible explanation of damage pattern by the whittier narrows, california, earthquake of 1 october 1987, *Bulletin of the Seismological Society of America*, **80**(1), 1–22.

- Keller, J. B., 1956. Diffraction of a convex cylinder, *Antennas and Propagation, IRE Transactions on*, **4**(3), 312–321.
- Lee, S.-J., Chan, Y.-C., Komatitsch, D., Huang, B.-S., & Tromp, J., 2009. Effects of realistic surface topography on seismic ground motion in the yangminshan region of taiwan based upon the spectral-element method and lidar dtm, *Bulletin of the Seismological Society of America*, **99**(2A), 681–693.
- Ma, S., Archuleta, R. J., & Page, M. T., 2007. Effects of large-scale surface topography on ground motions, as demonstrated by a study of the san gabriel mountains, los angeles, california, *Bulletin of the Seismological Society of America*, **97**(6), 2066–2079.
- Moczo, P., Bystrický, E., Kristek, J., Carcione, J. M., & Bouchon, M., 1997. Hybrid modeling of p-sv seismic motion at inhomogeneous viscoelastic topographic structures, *Bulletin of the Seismological Society of America*, **87**(5), 1305–1323.
- Nakamura, T., Takenaka, H., Okamoto, T., & Kaneda, Y., 2012. Fdm simulation of seismic-wave propagation for an aftershock of the 2009 suruga bay earthquake: Effects of ocean-bottom topography and seawater layer, *Bulletin of the Seismological Society of America*, **102**(6), 2420–2435.
- Nguyen, K.-V. & Gatmiri, B., 2007. Evaluation of seismic ground motion induced by topographic irregularity, *Soil dynamics and earthquake engineering*, **27**(2), 183–188.
- Pao, Y.-H. & Varatharajulu, V., 1976. Huygens’ principle, radiation conditions, and integral formulas for the scattering of elastic waves, *The Journal of the Acoustical Society of America*, **59**(6), 1361–1371.
- Pitarka, A., Irikura, K., Iwata, T., & Sekiguchi, H., 1998. Three-dimensional simulation of the near-fault ground motion for the 1995 hyogo-ken nanbu (kobe), japan, earthquake, *Bulletin of the Seismological Society of America*, **88**(2), 428–440.
- Razmkhah, A., Kamalian, M., & Alielahi, H., 2007. Low period amplification patterns of topographic features subjected to vertically propagating incident sv waves, in *4th International Conference on Earthquake Geotechnical Engineering*.
- Restrepo, D., Taborda, R., & Bielak, J., 2012. Three-dimensional nonlinear earthquake ground motion simulation in the salt lake basin using the wasatch front community velocity model, Tech. rep., Final technical report, USGS Award G10AP00077.
- Restrepo, D. L., 2013. *Effects of Topography on 3D Seismic Ground Motion Simulation with an Application to the Valley of Aburr’ a in Antioquia, Colombia*, Ph.D. thesis, Carnegie Mellon University.
- Restrepo, J. & Cowan, H., 2000. The eje cafetero earthquake, colombia of january 25 1999, *Bulletin of the New Zealand National Society for Earthquake Engineering*, **33**(1), 1–29.
- Sepúlveda, S. A., Murphy, W., Jibson, R. W., & Petley, D. N., 2005. Seismically induced rock slope failures resulting from topographic amplification of strong ground motions: The case of pacoima canyon, california, *Engineering geology*, **80**(3), 336–348.
- Takemiya, H. & Fujiwara, A., 1994. Sh-wave scattering and propagation analyses at irregular sites by time domain bem, *Bulletin of the Seismological Society of America*, **84**(5), 1443–1455.
- Trifunac, M., 1971. Surface motion of a semi-cylindrical alluvial valley for incident plane sh waves, *Bulletin of the Seismological Society of America*, **61**(6), 1755–1770.

- Trifunac, M., 1972. Scattering of plane sh waves by a semi-cylindrical canyon, *Earthquake Engineering & Structural Dynamics*, **1**(3), 267–281.
- Tselentis, G.-A. & Zahradnik, J., 2000. the athens earthquake of 7 september 1999, *Bulletin of the Seismological Society of America*, **90**(5), 1143–1160.